Noradrenaline and microglia maintain plasticity–rigidity balance to safeguard rapid emotional learning in the prefrontal cortex

Mio Tajiri[1, 3], Hidefumi Omi[1, 3], Airi Inoue[1], Hayato Etani[1], Takeshi Sawada[1], Yusuke Iino[1], Sho Yagishita[1, 2]*

[1] Laboratory of Structural Physiology, Center for Disease Biology and Integrative Medicine, Graduate School of Medicine, The University of Tokyo, Tokyo, Japan
[2] International Research Center for Neurointelligence (WPI-IRCN), UTIAS, The University of Tokyo, Tokyo, Japan
[3] These authors contributed equally to this work.

* Corresponding author: yagishita-tky@umin.ac.jp

Abstract

Balancing plasticity and rigidity is essential for brain function. While the neocortex typically shifts toward rigidity during development to preserve circuit integrity, certain forms of socially acquired emotional learning involve rapid remodeling in the medial prefrontal cortex (mPFC), raising the question of how such flexibility is achieved without compromising pre-existing representations. We found that activity-dependent dendritic spine enlargement is actively suppressed by microglia via a humoral factor in the adolescent mPFC. Noradrenaline lifted this suppression through cAMP signaling in microglia, permitting spine enlargement. Disruption of this noradrenaline-dependent pathway in the mPFC impaired the rapid acquisition of socially learned fear. Conversely, localized microglial ablation enhanced learning efficiency but disrupted emotional boundaries, inducing social fear learning to alter pain sensitivity. These findings demonstrate that noradrenaline and microglia regulate the plasticity–rigidity balance within an optimal range in the mPFC, enabling rapid social learning while safeguarding the functional segregation of emotional circuits.

Main

Synaptic plasticity enables the brain to learn from new experiences [1,2], but excessive plasticity can destabilize established neural circuits—a trade-off known as the plasticity–rigidity dilemma [3,4]. To manage this, plasticity must be tightly regulated in a region- and development-specific manner. In the neocortex, this balance shifts toward rigidity during maturation, favoring stable long-term memory storage at the expense of flexibility. This shift is reflected in the developmental decline in plasticity following the juvenile-to-adolescent transition [5–9], and in reliance on slower circuit-modification processes such as systems consolidation in the mature brain [3,4,10]. Yet, certain forms of socially acquired emotional learning occur within a single day and involve rapid remodeling of synaptic weights and neural activity in the medial prefrontal cortex (mPFC) [11,12]. The cellular mechanisms that enable such rapid learning while preserving the integrity of existing emotional circuits in the mature mPFC remain poorly understood.

The developmental decline of neocortical long-term potentiation (LTP) [5–9], a key form of synaptic plasticity, has traditionally been attributed to neuron-intrinsic changes [8,13,14]. However, the capacity for rapid synaptic remodeling in the mPFC requires core plasticity machinery to remain accessible under specific conditions. Increasing evidence instead points to a regulatory role for glial cells—particularly microglia—in shaping synaptic development [15,16], raising the possibility that they might contribute to the developmental attenuation of neocortical LTP. Moreover, recent studies show that noradrenaline (NA), a

classical neuromodulator known to promote plasticity and learning in the neocortex [17–23], also acts directly on microglia [24,25], suggesting a convergence of plasticity-related signals onto this cell type.

In this study, we tested whether dendritic spine enlargement, or structural LTP (sLTP) [26,27], in the mPFC declined during the transition from juvenile to adolescent stages, and identified a role for microglia in mediating this developmental suppression. Using two-photon glutamate uncaging, we induced sLTP by stimulating individual dendritic spines, which promotes glutamate receptor recruitment for synaptic potentiation [28–30]. We then examined whether NA can relieve microglial suppression of sLTP and whether this mechanism is engaged during the rapid learning through vicarious fear. Finally, we asked whether this plasticity-suppressing mechanism contributes to preserving functional integrity of emotional circuits during learning.

Microglial suppression of spine enlargement during development

We first characterized neocortical sLTP in adolescent and juvenile mice in the presence and absence of microglia. To ablate microglia, we locally injected clodronate into the mPFC, confirming nearly 90% ablation across a wide area of the mPFC 1–2 days after injection (Supplementary Figure 1A−C)[31]. To visualize microglia in acute slices, we generated double transgenic mice carrying a microglia-specific Cre driver allele, Tmem119-CreERT2, that maintains endogenous transmembrane protein 119 (Tmem119) gene expression via a P2A sequence [32], and an allele of a Cre-dependent

tdTomato reporter (Ai14), achieving more than 99% coverage in the mPFC (Figure 1A, Supplementary Figure 1D−G).

Coronal acute slices containing the mPFC were prepared from adolescent (5 to 7 weeks) and juvenile (2 to 3 weeks of age) mice. Layer 5 pyramidal neurons in the mPFC were subjected to whole-cell recordings and perfused with Alexa 488 to visualize dendritic spines using two-photon microscopy (980 nm) (Figure 1B−D, Supplementary Figure 1H,I). Small spines, located on the first to third branches of the apical dendrites (20 to 50 μm below the surface of the slice), were selected for plasticity induction. Caged glutamate (4 mM CDNI-Glu) was locally applied via a pressure pipette, and a two-photon laser was directed to the tip of the spine head (720 nm, 0.6 ms, 4−6 mW, adjusted depending on the depth of the dendrite). Uncaging stimulation of 3 or 4 spines, which elicited excitatory postsynaptic potential, was followed by action potentials within 10 ms, induced by current injections according to the STDP stimulation protocol (10 pairings at 10 Hz in a 10-s interval, repeated 15 times, Figure 1E, Supplementary Figure 1J) [33,34].

The STDP stimulation caused a transient increase in the spine volume, which returned to its initial level by 50 minutes in adolescent mice (Figure 1F; n = 5 dendrites, including 19 spines from 4 mice) but was sustained by 50 minutes in juvenile mice (2−3 weeks of age) (Figure 1G; n = 7 dendrites, including 28 spines from 3 mice). Ablation of microglia restored sustained sLTP in adolescent mice to levels resembling those in juveniles, while having little effect in the juvenile group (Figure 1H−K; clodronate in adolescent, n

95 = 7 dendrites, including 27 spines from 5 mice; clodronate in juvenile, n = 6 dendrites,
96 including 20 spines from 3 mice). The neighboring spines remained stable, indicating
97 that microglial ablation preserved stimulation-specific sLTP (Figure 1H, I). Another
98 microglia-ablating compound, PLX3397 [35], replicated the effect of clodronate in
99 adolescent mice (Supplementary Figure 1K−M; 6 dendrites, including 23 spines from 3
100 mice).

101 Plotting the volume changes against age reveals an age-dependent decline in sLTP in
102 the presence of microglia (Figure 1L; w/o clodronate, data shown in Figure 1F,G, and
103 additional data from mice aged 3−5 weeks; n = 16 dendrites, including 64 spines from
104 12 mice in total), but this decline was not observed in the absence of microglia (w/
105 clodronate, data shown in Figure 1H,I; n = 13 dendrites, including 47 spines from 8 mice
106 in total). Given the established correlation between dendritic spine volume and
107 glutamate sensitivity in the neocortex [36,37], these findings are consistent with previously
108 shown developmental decline in LTP [5,7,8] during the transition from juvenile to
109 adolescent. Our data further suggest that microglia acquire a suppressive role during
110 this developmental window, whereas pyramidal neurons retain an intrinsic capacity for
111 sLTP.

112 The absence of sLTP in adolescents might depend on stimulation strength. To
113 investigate this, we performed a plasticity induction experiment in magnesium-free
114 extracellular solution (Supplementary Figure 2A), which induces a strong Ca^{2+} influx
115 upon glutamate uncaging without action potentials, a widely adopted method for

116 inducing sLTP in the hippocampus [28–30]. Even under this magnesium-free condition,
117 glutamate uncaging (0.6 ms pulse, 5 Hz, 300 times) did not induce sLTP in slices from
118 adolescent mice (Supplementary Figure 2B,C; 7 dendrites, including 32 spines from 5
119 mice), but sLTP was induced in microglia-ablated slices (Supplementary Figure 2B,D,E;
120 5 dendrites, including 18 spines from 4 mice), replicating the results obtained with STDP
121 stimulation (Figure 1J).

122 The same magnesium-free protocol was sufficient to induce sLTP in the spines of
123 spiny-projection neurons in the nucleus accumbens, which is located in the same
124 section as the mPFC in adolescent mice (Supplementary Figure 2F,G; 5 dendrites,
125 including 19 spines from 4 mice). Given that the STDP stimulation protocol in the
126 nucleus accumbens requires G_s stimulation through dopamine or adenosine for sLTP
127 induction [33,34], the sufficiency of the magnesium-free condition for sLTP supports that
128 this stimulation protocol is stronger than the STDP protocol. In contrast to the mPFC of
129 adolescent mice, microglial ablation did not further promote sLTP in the nucleus
130 accumbens (Figure 1M, Supplementary Figure 2F,H; 5 dendrites, including 19 spines
131 from 4 mice), indicating regional differences in the microglial suppression mechanism.

132 Acute slice preparation might have altered microglial status [38]. A previous study on
133 microglia in acute slices reported a gradual increase in tissue ATP levels over 5 hours
134 after slice preparation, which caused morphological changes in microglia through
135 receptors such as $P2Y_{12}$ receptors [38]. Because we observed microglia ablation effects
136 only in the mPFC from adolescent mice, it is possible that microglia in the adolescent

137 PFC are more susceptible to these ATP-related alterations than those in the nucleus
138 accumbens or those in the juvenile PFC. We thus reanalysed the results with STDP
139 stimulation only by splitting the data into the first 2.5 hours and the later. However, we
140 found no significant difference between these two periods (Supplementary Figure 3A).
141 Additionally, the inhibition of $P2Y_{12}$ receptors did not induce plasticity with STDP alone
142 (Supplementary Figure 3B; 7 dendrites, including 27 spines from 5 mice). These data
143 indicate that the known alterations in microglia due to slice preparation cannot solely
144 account for the suppressive effect in the adolescent mPFC.

145 Together, these results indicate that during the transition from juvenile to adolescent
146 stages, microglia in the mPFC acquire a suppressive function that limits sLTP induction
147 across stimulation paradigms, while pyramidal neurons retain their capacity for plasticity.

148 Downstream signaling of microglial suppression

149 Having established that microglia suppress sLTP during adolescence, we next asked
150 how this suppression is implemented at the cellular and molecular level, which may
151 involve direct contact of microglia on spines or the release of humoral factors [39–48]. If
152 suppression requires physical contact, STDP stimulation should recruit microglial
153 processes around stimulated spines. In acute slices from Tmem119-CreERT2; Ai14
154 (Figure 2A), where more than 99% of microglia express tdTomato (Supplementary
155 Figure 1F), microglial protrusions were dynamically recruited to the site of adenosine
156 triphosphate (ATP) application via a pipette within 10 minutes (Figure 2B,C), as

157 previously reported [49]. When dendritic spines were simultaneously visualized with
158 microglia, less than 25% of dendritic spines were located near microglial processes
159 before stimulation (Supplementary Figure 4A−C). Unlike ATP application, STDP
160 stimulation did not recruit the microglial processes to the stimulated spines based on the
161 analyses of intensity (Figure 2C,D) or contact counts (Supplementary Figure 4C). Our
162 results therefore did not support a mechanism involving physical contact.

163 We thus tested whether humoral factors—tumor necrosis factor-α (TNF-α) and
164 interleukin-1β (IL-1β) —previously suggested to suppress LTP in the hippocampus [42–44]
165 and preferentially expressed in the microglia in the neocortex [50–54], would also suppress
166 sLTP in the mPFC. In microglia-ablated slices (Figure 2E), the presence of TNF-α (10
167 nM, bath) [55] but not IL-1β (1 ng/ml, bath) [43] suppressed STDP-induced sLTP (Figure
168 2E−G, Supplementary Figure 4E,F; TNF-α, n = 6 dendrites, including 21 spines from 4
169 mice; IL-1β, n = 6 dendrites, including 21 spines from 4 mice). TNF-α can signal through
170 a soluble form released after cleavage by TNF-α converting enzymes (TACE) or A
171 disintegrin and metalloprotease 17 (ADAM17) [56,57]. Inhibition of TACE/ADAM17 by
172 TAPI-0 (1 μM, bath) allowed sLTP in the presence of microglia (Figure 2H,
173 Supplementary Figure 5G; w/o TAPI-0, n = 8 dendrites, including 31 spines from 4 mice;
174 w/ TAPI-0, n = 6 dendrites, including 17 spines from 5 mice). Another class of TNF-α
175 inhibitor, pomalidomide (100 μM, bath) [58,59] also supported the involvement of TNF-α
176 signaling (Supplementary Figure 5H; n = 6 dendrites, including 21 spines from 4 mice).

177 Furthermore, the presence of TNF-α suppressed sLTP even in the juvenile mPFC
178 (Figure 2I, Supplementary Figure 4I,J; n = 7 dendrites, including 26 spines from 5 mice).

179 Given that microglia are a major source of TNF-α [52–54], these results suggest that
180 microglia suppress sLTP through the humoral action of TNF-α in adolescent mice,
181 possibly reflecting developmental changes in microglial properties [60].

182 Microglia-mediated actions of NA on spine enlargement

183 Since sLTP could be restored in adolescent slices by microglial ablation, we next tested
184 whether endogenous neuromodulatory signals could relieve this suppression under
185 physiological conditions. NA was a strong candidate, given its established role in
186 modulating neocortical synaptic plasticity [17,18,20] and its direct effects on microglial
187 function [24,25]. We thus locally delivered NA (50 μM) via a pressure pipette along with the
188 caged-glutamate starting 3−5 minutes before the onset of STDP stimulation to mimic
189 the transient release of NA seen *in vivo* [61] (Figure 3A−G). We found that the presence of
190 NA during STDP stimulation enhanced sustained sLTP in the stimulated spines up to 50
191 minutes (Figure 3B,C,G; STDP only, n = 9 dendrites, including 36 spines from 6 mice;
192 STDP with NA, n = 7 dendrites, including 22 spines from 6 mice; P = 0.028, post hoc
193 Steel's test against STDP after Kruskal–Wallis test against the following experiments
194 shown in Figure 3C−G, Supplementary Figure 5A−H). In contrast, the presence of
195 dopamine (50 μM, puff), another catecholamine that affects spine dynamics *in vivo* [62],

196 did not promote sLTP, unlike in the nucleus accumbens [34] (Figure 3G, Supplementary
197 Figure 5A; n = 6 dendrites, including 24 spines from 4 mice; *P* = 1.00).

198 Next, we characterized downstream signaling of NA by pharmacologically perturbing
199 G_s-coupled β adrenergic receptors (ARs), which stimulate cAMP production, and
200 phosphodiesterase (PDE), which degrades cAMP, given that the β-ARs-cAMP-PKA
201 pathway generally facilitates LTP [63,64]. RNA-seq data provide comprehensive
202 information on the cellular distribution of β-ARs in the neocortex [50,65], and show that β_1-
203 and β_3-ARs are primarily localized to neurons and astrocytes, while β_2-ARs are
204 predominantly expressed in microglia. Bath application of ICI118,551 (1 μM, β_2 inverse
205 agonist) blocked NA-enhanced sLTP (Figure 3D,G, Supplementary Figure 5B, n = 6
206 dendrites, including 23 spines from 3 mice; *P* = 1.00), whereas the bath application of
207 metoprolol (1 μM, β_1 inverse agonist) did not (Figure 3D,G, Supplementary Figure 5C, n
208 = 7 dendrites including 28 spines from 5 mice; *P* = 0.038). Furthermore, puff application
209 of clenbuterol (10 μM, a β_2 agonist) was able to reproduce the effect of NA on sLTP
210 (Figure 3E, Supplementary Figure 5D, n = 7 dendrites, including 23 spines from 7 mice;
211 *P* = 0.028). Among the PDE families, PDE3b is preferentially expressed in microglia [66],
212 while PDE4 subtypes are expressed in pyramidal neurons [50]. We hypothesized that the
213 presence of a PDE inhibitor could substitute for the effects of G_s-coupled receptor
214 stimulation. STDP alone caused sLTP in the presence of cilostamide (1 μM bath, PDE3
215 inhibitor) (Figure 3F,G, Supplementary Figure 5E; n = 7 dendrites, including 27 spines
216 from 5 mice; *P* = 0.028). In contrast, rolipram (1 μM bath, PDE4 inhibitor), at a
217 concentration known to enhance hippocampal LTP [67], did not facilitate sLTP (Figure

218 3F,G, Supplementary Figure 5F; n = 6 dendrites, including 24 spines from 3 mice; *P* =
219 0.84). These pharmacological results are consistent with a hypothesis that NA acted via
220 β_2-ARs on microglia to promote sLTP.

221 Further pharmacological experiments confirmed that the NA-dependent sLTP was
222 abolished in the presence of D-AP5 (50 μM, bath application; NMDA receptor
223 antagonist) (Figure 3G, Supplementary Figure 5G; n = 7 dendrites, including 27 spines
224 from 6 mice; *P* = 0.99), or PKI (10 μM, a PKA inhibitor, in the intracellular solution)
225 (Figure 3G, Supplementary Figure 5H; n = 6 dendrites, including 23 spines from 4 mice;
226 *P* = 0.98). We then tested whether expressing the CaMKII inhibitory peptide
227 (autocamtide-2-related inhibitory peptide, AIP) prevents sLTP[33,68]. We delivered AIP
228 through an AAV vector under CaMKII promoter (Figure 3H). NA-dependent sLTP was
229 observed in neurons expressing the control vector (Figure 3I, Supplementary Figure 5I;
230 n = 6 dendrites, including 24 spines from 6 mice) but was blocked in AIP-expressing
231 neurons (Figure 3I, Supplementary Figure 5J, n = 7 dendrites, including 23 spines from
232 4 mice). These data indicate that the essential signaling mechanisms for sLTP are
233 similar to those described in the hippocampus and striatum [33,34,69].

234 Using microglia-specific chemogenetic inhibition of cAMP signaling, we further
235 addressed whether microglia mediate the action of NA (Figure 3J). We used
236 double-transgenic mice expressing hM4Di, a $G_{i/o}$-coupled receptor that suppresses
237 cAMP production in a Cre-dependent manner (R26-LSL-hM4Di-mCitrine)[70] under the
238 control of Tmem119-CreERT2 (Figure 3K). This combination has been employed in

239 recent studies to modulate microglial functions [71]. The R26-LSL-hM4Di-mCitrine line is
240 known to exhibit leak expression, which was observed in 3% of cells in the mPFC
241 (Supplementary Figure 6A−C). After repeated intraperitoneal tamoxifen injections
242 (Supplementary Figure 6D), we confirmed the expression of the chemogenetic probe in
243 microglia in fixed slices, along with leak expression in other cells (Supplementary Figure
244 6E,F).

245 In acute slices, we recorded from pyramidal neurons without detectable mCitrine
246 fluorescence and applied a potent hM4Di actuator, deschloroclozapine (DCZ, 100
247 nM)[72–74] in the bath. We found that the presence of Cre prevented sLTP induction by
248 STDP stimulation with NA (Figure 3M−O; without Cre, n = 6 dendrites, including 24
249 spines from 3 mice; with Cre, n = 6 dendrites, including 24 spines from 4 mice).
250 Importantly, STDP-induced sLTP was fully preserved in non-Cre slices from the same
251 double-transgenic mice (Figure 3C vs. Figure 3M), indicating that leak expression and
252 potential off-target effects of DCZ did not impair plasticity. Thus, these results indicate
253 that microglial cAMP signaling mediates the NA enhancement effects on spine
254 enlargement.

255 Microglial ablation experiments suggested that TNF-α suppresses plasticity downstream
256 of microglia (Figure 2G, Figure 3J), indicating that TNF-α may interfere with NA's effects
257 on plasticity. Supporting this, TNF-α application reduced NA-enabled sLTP induced by
258 STDP (Figure 3P, Supplementary Figure 6G, w/o TNF-α, n = 6 dendrites, 24 spines
259 from 5 mice; w/ TNF-α, n = 8 dendrites, 31 spines from 5 mice).

260 Collectively, our *ex vivo* experiments demonstrate that, although microglia adopt a
261 suppressive role in plasticity following brain maturation, NA can counteract this effect
262 via β_2-ARs and cAMP signaling within microglia, thereby enabling sLTP in the mPFC.

263 NA-dependent plasticity signaling in rapid social learning

264 We next tested whether the NA-dependent plasticity pathway contributes to the rapid
265 acquisition of social learning using the observational fear learning (OFL) paradigm
266 [11,75–77]. Pairs of male adolescent mice (6–7 weeks old) were co-housed for 4 days. On
267 day 1, one mouse (the observer) received two foot shocks (0.4 mA, 2 s) in a
268 conditioning chamber (Figure 4A). On day 2, the cage mate (the demonstrator) was
269 placed in the same chamber and exposed to 24 tone–shock pairings (6 kHz tone, 5 s;
270 0.7 mA shock, 2 s). Tone and shock presentations elicited transient freezing in
271 observers regardless of demonstrator presence, likely due to novelty, but sustained
272 freezing occurred only when observers witnessed their cage mate being shocked
273 (Figure 4B, Supplementary Figure 7A; with demonstrator, n = 8; without, n = 6). On day
274 3, memory was tested by presenting the tone alone (6 kHz, 60 s, 3 trials). Observer
275 mice exhibited robust freezing during tone presentation, but only if they had previously
276 witnessed the demonstrator being shocked (Figure 4C, Supplementary Figure 7B).
277 Although female mice also acquired OFL, their freezing responses on day 2 were
278 weaker (Supplementary Figure 7C–F, n = 6), and because day 2 freezing was used as

279 an internal reference for subsequent experiments, females were excluded from further
280 testing.

281 We then assessed NA dynamics in the mPFC using the GPCR-based fluorescent
282 sensor GRAB-NE_{2m} [78]. An AAV expressing GRAB-NE_{2m} under the synapsin promoter
283 was injected into the right mPFC, and fluorescence was recorded via an implanted
284 optical fiber (Figure 4D). As a positive control, direct foot shock elicited a transient
285 fluorescence increase that peaked within seconds and decayed over tens of seconds
286 (Supplementary Figure 7G,H; *n* = 5 mice), consistent with prior reports [79]. During OFL,
287 GRAB-NE_{2m} signals in observer mice increased transiently during the 240-second shock
288 period delivered to demonstrator mice on day 2 (Figure 4E, Supplementary Figure 7I, n
289 = 6 mice), consistent with noradrenergic axon activity patterns [61]. In contrast, no signal
290 increase was observed on day 3 during cue-driven recall (Supplementary Figure 7J–L).
291 These results indicate that demonstrator distress evokes a sustained, minute-scale NA
292 response in the mPFC, resembling the timing of NA application in slice experiments
293 (Figure 3A,C). Although GRAB-NE_{2m} was expressed in neurons, this volume-transmitted
294 NA signal likely reflects levels accessible to microglia.

295 To test the role of β_2-ARs in the acquisition of OFL, we bilaterally infused ICI118,551 or
296 ACSF as a vehicle control into the mPFC on day 2 through cannulas implanted in
297 advance (Figure 4F). The infusion of ICI118,551 did not affect the expression of the
298 freezing response during conditioning but subsequently inhibited freezing on day 3
299 (Figure 4G,H, Supplementary Figure 7M,N, Vehicle, n = 7 mice; ICI118,551, n = 6 mice).

300 Because freezing during conditioning typically correlates with memory strength [80], this
301 dissociation suggests that β_2-AR blockade selectively impaired memory formation rather
302 than the expression of fear. Combined with previous reports that non-selective β-AR
303 antagonists suppress vicarious fear responses [61], these findings suggest a preferential
304 role for β_2-AR in the mPFC for memory formation, while β_1-AR may contribute more
305 directly to fear expression.

306 Given that AIP prevented sLTP induction, we expressed AIP bilaterally in the mPFC as
307 well as anterior cingulate cortex (ACC) (Figure 4I, Supplementary Figure 8A), which did
308 not affect conditioning on day 2 (Figure 4J, Supplementary Figure 8B, mCherry, n = 10
309 mice; AIP, n = 8 mice) but impaired freezing on day 3 test (Figure 4K, Supplementary
310 Figure 8C), similar to the β_2 blocker experiment.

311 These results indicate that the NA-dependent plasticity pathway in the mPFC is required
312 for the rapid formation of social fear learning in adolescent male mice.

313 Microglial role in rapid social learning

314 Based on our slice experiments (Figure 1J), we predicted that microglial ablation in the
315 mPFC would enhance the acquisition of observational fear learning (OFL). Clodronate
316 was unilaterally injected into the right mPFC on day 0 via a glass pipette, with spread
317 extending into the anterior ACC by the following day (Figure 5A–C, Supplementary
318 Figure 9A). To avoid ceiling effects during OFL, demonstrator mice received
319 lower-intensity foot shocks (0.2 mA) with fewer repetitions (12 trials) on day 2 (Figure

320 5A). Under this subthreshold protocol, control observer mice showed freezing during
321 conditioning (Figure 5D, Supplementary Figure 9B) but responded only modestly to the
322 tone during testing on day 3 (Figure 5E, Supplementary Figure 9C). Microglial ablation
323 did not affect freezing during conditioning (Figure 5D, Supplementary Figure 9B;
324 Vehicle, *n* = 7 mice; Clodronate, *n* = 6 mice) but significantly enhanced freezing on day
325 3 (Figure 5E, Supplementary Figure 9C). These results support the hypothesis that
326 microglial ablation facilitates learning rather than simply enhancing threat sensitivity.

327 We next asked whether enhanced plasticity in the absence of microglia might lead to
328 the recruitment of task irrelevant emotion-related circuits. Pain is an emotional function
329 regulated in part by the mPFC, including the ACC, where synaptic potentiation
330 modulates sensitivity [81,82]. Notably, some neurons in this region encode overlapping
331 representations of pain and vicarious fear [83], suggesting that precise plasticity control is
332 required to update vicarious fear memories without interfering with pain-related
333 processing. We therefore hypothesized that OFL in the absence of microglia could alter
334 pain sensitivity in a learning-dependent manner. To assess pain sensitivity, we used the
335 thermal place preference (TPP) test [84], in which mice were allowed to freely explore two
336 plates maintained at different temperatures. Avoidance of the warmer plate serves as a
337 readout of thermal nociception. Control mice showed a modest tendency to avoid 40 °C,
338 no discrimination between identical 30 °C plates, and consistent avoidance of the 50 °C
339 plate (Supplementary Figure 9D; *n* = 8 mice).

We repeated OFL using the standard protocol to compare animals with and without microglial ablation in the right mPFC (Figure 5F). Freezing levels on both day 2 and day 3 were comparable between groups, consistent with a ceiling effect under these conditions (Figure 5G, H, Supplementary Figure 9E–G; Vehicle, *n* = 7 mice; Clodronate, *n* = 7 mice). We then assessed thermal sensitivity using the TPP test (30 °C vs. 40 °C) and found that vehicle-injected mice did not differ from naïve controls ("No task"), indicating that OFL alone did not alter thermal nociception (Figure 5I). In contrast, mice that underwent OFL in the absence of microglia (clodronate-injected) showed significantly increased thermal aversion (Figure 5I). This effect was absent in clodronate-injected mice exposed to the task chamber without a demonstrator (Figure 5G–I, Supplementary Figure 9F, G; Clodronate Dem (−), *n* = 7 mice). These findings indicate that, in the absence of microglia, social fear learning can aberrantly enhance pain sensitivity, inducing experience-dependent cross-talk between emotional circuits.

To determine whether enhanced thermal aversion reflects a unique requirement for prefrontal synaptic plasticity during social learning, we performed auditory fear conditioning using direct fear experience. Mice received four tone–shock pairings on day 1 (Supplementary Figure 8D), followed by tone presentations on day 2. In contrast to its effect on OFL, CaMKII inhibition via AIP expression in the mPFC did not impair the rapid acquisition of fear conditioning from direct experience (Supplementary Figure 8E, F; mCherry, *n* = 7 mice; AIP, *n* = 5 mice), consistent with previous findings of delayed synaptic remodeling in the mPFC [10]. Likewise, microglial ablation in the right mPFC did not affect conditioning or subsequent thermal sensitivity (Figure 5K, Supplementary

362 Figure 9H, I; Vehicle, *n* = 7 mice; Clodronate, *n* = 8 mice). These findings highlight a
363 selective requirement for prefrontal plasticity mechanisms in supporting rapid learning
364 from social—but not direct—fear experiences.

365 Discussion

366 We found that microglia suppress sLTP in the mPFC during the transition from juvenile
367 to adolescent stages. Although microglial ablation restored plasticity to juvenile levels
368 and enhanced social fear learning, it also caused vicarious fear learning to spill over into
369 heightened pain sensitivity, suggesting that the rigidity control by microglia safeguarding
370 the functional separation of emotional circuits. Under physiological conditions, NA
371 facilitates plasticity by counteracting the microglial mechanisms via β_2-adrenergic
372 receptors and cAMP signaling, enabling rapid social learning without affecting pain
373 sensitivity. These findings demonstrate that NA and microglia jointly regulate prefrontal
374 synaptic plasticity within an optimal range, balancing learning efficiency with the
375 preservation of emotional boundaries.

376 Using two-photon glutamate uncaging, we isolated the postsynaptic component of
377 neocortical synaptic plasticity and confirmed its developmental decline during the
378 transition from juvenile to adolescent stages, consistent with previous reports [5–9]. In
379 contrast to earlier models attributing this decline to neuron-intrinsic mechanisms [7,8,13,14],
380 our results show that microglia play a critical role, likely through the humoral release of
381 TNF-α, while pyramidal neurons retain their plastic potential at least until 7 weeks of age
382 (Figure 1I). Although we cannot fully exclude the possibility that microglial suppression

383 of sLTP reflects artefacts during slice preparation, behavioral learning experiments with
384 β_2-ARs inhibition and microglial ablation are consistent with the microglial suppression
385 model. Elevated plasticity during the juvenile period may promote adaptive circuit tuning
386 [1,14], but also risks destabilizing mature networks, as predicted by modeling studies [3,4]. By
387 ablating microglia, we directly tested this hypothesis, demonstrating that microglia
388 protect circuits from excessive experience-driven modifications in the mature mPFC.
389 Unlike inhibitory mechanisms that irreversibly suppress plasticity after the critical period
390 closure [85], microglial suppression is unique in that it can be reversed by a single
391 physiological signal of NA.

392 NA enhances synaptic plasticity in the adolescent mPFC by counteracting
393 microglia-dependent suppression, extending prior findings on the role of
394 NA/β-AR/cAMP/PKA signaling in promoting neocortical LTP [17–20,86,87]. Consistent with
395 earlier work showing that cAMP/PKA signaling in neurons is essential for LTP [88] and
396 sLTP [34,89], we found that NA-dependent neocortical sLTP required PKA activity in
397 pyramidal neurons, as shown by sLTP inhibition when the PKA inhibitor PKI was
398 included in the recording pipette (Figure 3G). However, neuronal PKA activation alone
399 was insufficient to induce sLTP in the mature mPFC, which additionally required
400 β_2-ARs/cAMP signaling in microglia to relieve suppression. Given that TNF-α mediates
401 this suppression, NA may act to suppress TNF-α release, consistent with its known
402 immunomodulatory effects in monocytes [90,91] and macrophages [92,93].

The plasticity pathway involving NA, β_2-ARs, and CaMKII in the mPFC is necessary for the rapid establishment of social learning, supporting the hypothesis that the mPFC undergoes active synaptic remodeling during observational learning rather than merely relaying social information. In contrast, this pathway was dispensable for learning from direct experience, consistent with prior reports showing that mPFC synaptic potentiation emerges only days after direct conditioning [10]. NA levels rise in the mPFC during both observation and direct shock (Figure 4E, Supplementary Figure 7H), indicating that NA release alone does not account for the selective engagement of plasticity during social learning. Instead, we propose that distinct patterns of glutamatergic activity during social observation uniquely recruit mPFC plasticity. Supporting this, microglial ablation enhanced pain sensitivity only after social—but not direct—fear learning (Figure 5I, K), suggesting that excessive plasticity altered representations beyond the social domain. Given that mPFC neurons often exhibit mixed selectivity [94], with overlapping representations of vicarious fear and pain-related signals [83], plasticity must be tightly constrained. NA–microglia interactions may thus gate synaptic modifications within an optimal range, enabling selective updating for social emotional memory while preserving the integrity of other affective representations.

A similar NA–microglia-dependent plasticity pathway may operate in other cortical regions. Rapid spine remodeling has been observed in motor and sensory cortices [95,96], where sLTP is limited under glutamatergic stimulation alone [97,98], suggesting a possible role for NA-mediated gating. The sustained elevation of NA over minutes during learning (Figure 4E) contrasts with the phasic, subsecond dynamics of striatal dopamine

involved in reinforcement learning [33,34], indicating that neocortical learning may rely on a distinct computational algorithm. While microglia suppressed plasticity and learning in the mPFC, microglia in the hippocampus have been shown to facilitate fear conditioning driven by direct experience [99,100], further highlighting region-specific roles of microglia in plasticity and learning.

In conclusion, microglia safeguard emotional circuitry while enabling rapid social learning by finely regulating synaptic plasticity in the mature mPFC. Incorporating this microglial gating mechanism into computational models of learning may offer new insights into how neural circuits balance plasticity with rigidity [4]. The transition from juvenile to adolescent stages represents a critical period for the emergence of psychiatric disorders [101], during which microglia have been increasingly implicated in pathophysiology [102]. Defining how microglia regulate prefrontal plasticity and emotional learning in pathological contexts may offer a foundation for understanding the cellular bases of psychiatric vulnerability.

Acknowledgement

We thank Y. Li for the GRAB sensor plasmid; K. Hagihara, R. Hira, H. Kasai, A. Kumar, T. Masuda, J. Nagai, T. Okuyama, K. F. Tanaka, and A. Uematsu for helpful discussions; and M. Asaumi, A. Abe, R. Miyashita, A. Kurabayashi, and A. Nishikawa for technical assistance. This work was supported by Brain/MINDS (19dm0207069 to S.Y.) and Multidisciplinary Frontier Brain and Neuroscience Discoveries (Brain/MINDS 2.0) (JP23wm0625001, JP24wm0625308, JP24wm0625101 to S.Y.) from AMED;

Grants-in-Aid (JP21H05171, JP21H05176, and 24K02115 to S.Y.) from JSPS; Moonshot R&D (JPMJMS2021 to S.Y.) from JST; The Uehara Memorial Foundation (to S.Y.); and The Mitsubishi Foundation (to S.Y.).

Author contribution

S.Y. conceptualized the study. M.T. performed and A.I. and Y.I. assisted slice experiments. H.O. performed and T.S. assisted behavioral experiments. H.E. produced AAV vectors. All the authors interpreted the data. S.Y., M.T and H.O. drafted and all the authors edited the manuscript.

Declaration of interests

The authors declare no competing interests.

Methods

Animals

C57BL/6J mice were purchased from Sankyo lab service. Tmem119-CreERT2 mice [C57BL/6-Tmem119 (Cre/ERT2) Gfng/J; stock #031820][32], Ai14 mice [B6.Cg-Gt (ROSA) 26Sortm14 (CAG-tdTomato) Hze/J; stock #007914] and R26-LSL-hM4Di-mCitrine mice [B6.129-Gt (ROSA) 26Sortm1 (CAG-CHRM4*,-mCitrine) Ute/J; stock #026219][70] were obtained from the Jackson Laboratory. Mice were housed on a 12-hour/12-hour light/dark cycle with *ad libitum* access to food and water. All animal experiments were approved by the Animal Experimental Committee of the Faculty of Medicine at the University of Tokyo.

Plasmids and adeno-associated viruses (AAV)

For AAV production, we prepared the following constructs using PCR and Infusion (Takara): pAAV-CaMKII(0.3)-FAS-NLS-mCherry-W and pAAV-CaMKII(0.3)-FAS-NLS-mCherry-P2A-AIP-W, where FAS is loxP-FAS that has no effect in this study, NLS is nuclear localisation sequence, AIP autocamtide 2-related inhibitory peptide (KKALRRQEAVDAL), and P2A a self-cleaving peptide or obtained a plasmid from Addgene (pAAV-hSyn-GRAB-NE2m-W, #208686)[78]. AAVs were produced and their titres were measured as described previously [103]. Briefly, AAV expression vector, pHelper (Stratagene) and either pRepCap AAV5 (Applied Viromics) or pUCmini-iCAP-PHP.eB (#103005, Addgene) were transfected into HEK293 cells

477 (AAV293, Stratagene). After three days, cells were harvested and AAV were purified
478 twice using ultracentrifuge with iodixanol. The titres for AAV (genome copies, GC) were
479 estimated using quantitative PCR.

480 *Surgery*

481 For AAV injection, mice were anesthetized with isoflurane (1-3%) and placed in a
482 stereotaxic frame (Narishige). AAVs were bilaterally (AIP experiments) or unilaterally
483 (photometry experiments) infused into the mPFC (AP +1.8 mm, ML ±0.3 mm, DV +2.4
484 mm for slice experiments; AP +1.1 mm, ML ±0.3 mm, DV +2.0 mm for behavioral
485 experiments) and using a glass needle at a rate of 100 nl/min. Either of following AAVs
486 was infused 1 μl per hemisphere:

487 - AAV2/5: CaMKII(0.3)-FAS-NLS-mCherry-W (2.0×10^{13} GC/ml)
488 - AAV2/5: CaMKII(0.3)-FAS-NLS-mCherry-P2A-AIP-W (2.0×10^{13} GC/ml)
489 - AAV2/PHP.eB: hSyn-GRAB-NE_{2m}-W (2.0×10^{13} GC/ml)

490 The glass needle was withdrawn 5 minutes after the end of the infusion. For photometry
491 experiments, the optical cannula (NA 0.5, 200 μm in diameter, 3.0 mm in length, RWD)
492 was placed in the same coordinate to the injection. The mice were allowed to recover in
493 their home cages for at least 2 weeks before slice or behavioral experiments.

494 For slice experiments with microglia ablation [31], 1 μl of 7 mg/ml clodronate (HY-B0657A,
495 MCE) or clophosome (F70101C-N, Funakoshi) was injected following the same protocol

496 used for virus injections. As vehicle controls, either ACSF or liposome (F70101-N,
497 Funakoshi) was used. Since no significant difference was observed between the effects
498 of clodronate and clophosome, the results were pooled for analysis.

499 For behavioral experiments with microglia ablation, 0.5 μl of 3 mg/ml clodronate was
500 injected into the right mPFC (AP +1.1 mm, ML +0.3 mm, DV +2.0 mm).

501 For drug cannula placement for behavioral experiments, a double cannula (26-gauge,
502 Plastic One or RWD) was placed to target the bilateral mPFC (AP +1.1 mm, ML ±0.3
503 mm, DV +2.0 mm).

504 *Acute slice preparation*

505 Acute coronal slices (280 μm thick) containing the mPFC were obtained from 2- to 7-
506 week-old female and male mice. Mice were anesthetized using isoflurane and then
507 perfused transcardially by ice-cold solution (220 mM sucrose, 3 mM KCl, 8 mM $MgCl_2$,
508 1.25 mM NaH_2PO_4, 26 mM $NaHCO_3$, and 25 mM glucose) and were quickly
509 decapitated. Brains were removed and sliced with a microtome (VT1200, Leica). The
510 slices were incubated at 34°C for 30 minutes and then at room temperature in ACSF
511 (125 mM NaCl, 2.5 mM KCl, 1 mM $CaCl_2$, 2 mM $MgCl_2$, 1.25 mM NaH_2PO_4, 26 mM
512 $NaHCO_3$, 20 mM glucose, and 200 μM Trolox (238813, Merck) which was bubbled with
513 95% O_2 and 5% CO_2. Then, the slices were transferred to a recording chamber and
514 perfused with the ACSF solution described above, except using 2 mM $CaCl_2$ and 1 mM

515 $MgCl_2$, or 2 mM $CaCl_2$ and 0 mM $MgCl_2$ for magnesium-free experiments. All
516 physiological experiments were performed at 30–32 °C.

517 *Structural plasticity in slices*

518 Two-photon imaging of dendritic spines was performed using an upright microscope
519 (BX61WI, Olympus) equipped with an FV1200 laser-scanning system (Olympus) with
520 GaAsP photomultiplier tubes (Hamamatsu Photonics) and a water-immersion objective
521 lens (NA 1.0, LUMPlanFI/IR, ×60, Olympus). The system included two mode-locked,
522 femtosecond-pulse Ti:sapphire lasers (MaiTai, Spectra Physics). One was set at a
523 wavelength of 720 nm for the uncaging of glutamate and the other was set at 980 nm
524 for imaging. Fluorescence intensities of green and red fluorophores were detected
525 through 500−550 nm (F03-525/50, Semrock) and 600−680 nm (ET642/80m, Chroma)
526 filters, respectively after a dichroic mirror (T585lpxr, Chroma).

527 For whole-cell recordings, the patch pipettes (5−8 MΩ) were filled with a solution
528 containing 120 mM potassium gluconate, 20 mM KCl, 10 mM disodium
529 phosphocreatine, 4 mM ATP (magnesium salt), 0.3 mM GTP (sodium salt), 10 mM
530 HEPES, 50 μM Alexa 488 hydrazide (A10436, Thermo Fisher Scientific) or Alexa 594
531 hydrazide (A10438, Thermo Fisher Scientific) and 5 μM β-actin (APHL99,
532 Cytoskeleton), whose pH and osmolarity were adjusted to 7.25 and 275−280 mOsm by
533 KOH and sucrose, respectively. We did not include Ca^{2+} buffer in the internal solution.
534 For pharmacological experiments, protein kinase A inhibitor (10 μM, 6211, Tocris) was
535 included in the pipette. The cells were voltage-clamped at −70 mV except during

536 stimulation. Cells were discarded if spontaneous action potentials were observed during
537 the stimulating period.

538 CDNI-glutamate (4 mM, Nard Institute) was locally puffed from a pipette. In experiments
539 with L-noradrenaline hydrochloride (50 μM, #74480, Merck), dopamine hydrochloride
540 (50 μM, D5662, Fujifilm) and clenbuterol (10 μM, C2691, TCI), the reagents were also
541 included in the puff pipette solution. For glutamate uncaging, a 720-nm laser was set to
542 4−6 mW, depending on the depth to compensate for the decline in stimulation efficiency.
543 Excitatory postsynaptic currents (EPSCs) were recorded by stimulating 3 to 4 spines for
544 0.6 ms for each while cells were clamped at -70 mV. After confirming the successful
545 induction of EPSCs, structural plasticity was induced by a spike-timing-dependent
546 plasticity (STDP) protocol as previously described [33,34]. Briefly, one burst was composed
547 of three back-propagating action potentials (bAPs, at 100 Hz) preceded by a single
548 EPSP (Δt = +10 ms) induced by two-photon uncaging of CDNI-glutamate. One train of
549 STDP consisted of ten bursts repeated at 10 Hz. Fifteen trains of stimulation were
550 repeated at 0.1 Hz. APs were induced by injection of a depolarizing current of 1.5−2.0
551 nA for 2 ms. Dendrites containing spines within 100 μm of the soma and 20−50 μm in
552 depth were subjected to plasticity induction. For each experiment, three to four spines
553 were stimulated.

554 In experiments with D-AP5 (50 μM, #0106, Tocris Bioscience), ICI118,551 (1 μM,
555 ab120808, Abcam), metoprolol (1 μM, M5391, Merck), cilostamide (1 μM, S5806,
556 Selleck), rolipram (1 μM, #180-01411, Fujifilm), deschloroclozapine (DCZ, 100 nM,

557 #7193, Tocris)[72–74], TAPI-0 (1 μM, 579050, Calbiochem), pomalidomide (100 μM, P2074,
558 TCI), mouse recombinant tumor necrosis factor-α (TNF-α, 10 nM, 207-13463, Fujifilm),
559 or mouse recombinant interleukin-1β (IL-1β, 1 ng/ml, 094-04681, Fujifilm), slices were
560 constantly perfused with the reagent throughout the series of imaging.

561 In acute slices following clodronate injection, regions lacking microglia were identified by
562 the absence of fluorescence in transgenic mice expressing tdTomato in microglia. In
563 some experiments, clodronate or vehicle was injected into wild-type mice. Even in these
564 wild-type mice, the ablation site was reliably identified by a needle trace, and cells were
565 recorded within 200 μm of the trace. The site was later confirmed histologically through
566 immunostaining.

567 *Observational fear learning*

568 Before performing observational fear learning, mice were co-caged for 4 days in their
569 home cage. On day 1, an observer mouse was placed in a conditioning chamber with a
570 stainless-steel rod floor (30 cm × 30 cm, Melquest) for 5 minutes, during which two
571 uncued footshocks (0.4 mA, 2 s each, 1-minute interval; shock generator, No.
572 SG1000-S, Melquest) were delivered. The mice were then returned to their home cage.

573 On day 2, the mice were placed in a different chamber (17 cm × 35 cm, Melquest),
574 which was divided into two sections: one with a plastic floor for the observer mouse, and
575 the other with a metal rod floor for a naive cagemate (the demonstrator). After 5 minutes
576 of habituation, the demonstrator mouse received 24 successive cued footshocks (tone:

577 6 kHz, 80−85 dB, 5 s; footshock: 0.7 mA, 2 s, 10-second interval). The observer mouse
578 was then returned to its home cage with its cagemate.

579 On day 3, memory was assessed by placing the observer mice back into the
580 observation chamber in the same context and presenting three cues (6 kHz tone; 80−85
581 dB; 60 s; with intervals of 165 s and 177 s). For subthreshold conditioning, 12 cued
582 weak foot shocks (0.2 mA, 2 s each) were presented to the observer mice on day 2.

583 The stimulus presentation was controlled by triggers generated through a DAQ board
584 (PCIe-6223, National Instruments) using custom-written software. The entire session
585 was recorded with a camera (CS235MU, Thorlab) at 20 fps, synchronized with the
586 stimulus presentation through the DAQ board.

587 For experiments involving drug infusion, the double cannula was connected to a syringe
588 (1801RN, Hamilton) via a tube containing either the β_2 blocker ICI118,551 (200 μM in
589 ACSF) or ACSF alone, while the mice were under anesthesia (1% isoflurane, Fujifilm).
590 The drug was infused at a rate of 0.1 μl/min, with a total volume of 1 μl, controlled by a
591 microsyringe pump (Legato 111, KD Scientific). Mice were allowed to recover for at least
592 30 minutes before undergoing conditioning.

593 For experiments involving clodronate, mice were euthanized a few days after the
594 memory test, and the patterns of ablation were assessed by immunohistochemistry.

Auditory conditioning with direct fear experience

On day 1, mice were placed in the conditioning chamber (metal rod floor and plexiglass chamber, stripe wall) for 3 minutes and subsequently received pairs of cues (6kHz tone, 20 s) and footshocks (0.7 mA, 1 s at the offset of tone) for 4 times with 60−79 s pseudo-randomized intervals. On day 2, mice were placed in another context (dot wall) and the cues were presented 4 times with 60−77 s pseudo-randomized intervals. The entire session was recorded with a camera (CS235MU, Thorlab) at 20 fps.

Thermal place preference test

Thermal preference behavior was assessed using a two-zone apparatus consisting of two adjoining aluminum plates (100 mm × 100 mm each), whose temperatures were independently controlled. The plates formed a continuous flat floor joined by a copper bridge and enclosed by clear acrylic walls (400 mm high), creating a test arena measuring 220 mm × 100 mm. Mice were recorded at 20 frames per second using a side-mounted video camera.

Prior to testing, mice were habituated to the behavioral room for 10 minutes. Each mouse was then placed into the apparatus, with one plate set to a neutral 30 °C and the other to 40 °C. The side assignment of the warmer plate was counterbalanced across animals. Mice were recorded for 10 minutes, and the final 5 minutes were used to calculate place preference [84]. Mice that urinated during the session were excluded from analysis.

615 *Fiber photometry*

616 A 470 nm LED (M470F3, Thorlabs) and 405nm LED (M405F1, Thorlabs) were pulsed (2
617 ms at 20 Hz, 10 to 15 μW) with shifting 20 ms in order to separate the excitation timing.
618 The excitation light was passed through an excitation filter (ET405/20x; PCR47030x,
619 Chroma Technology), dichroic mirrors (DMLP425, Thorlab; ZT488rdc, Chroma
620 Technology), an objective lens (Olympus, UPlanFLN 20x), then through a rotary joint
621 (RJ-1, Thorlabs) and finally into a low-autofluorescence patch cord (custom made,
622 Thorlabs) connected to the optical implant in the mouse. Emission light was collected
623 through the same patch cord, then passed back through the cube with the dichroic
624 mirror and a fluorescence filter (ET525/50m, Chroma Technology), and then detected by
625 a GaAsP detector (PMT2101/M, Thorlabs). Voltages from the photomultiplier were
626 bandpass filtered (1k Hz) and collected through the DAQ board used for the behavioral
627 experiments.

628 *Drug administration*

629 For adolescent mice, Tamoxifen (HY-13757A, MedChemExpress, 100 mg/kg body
630 weight) dissolved in corn oil was administered via intraperitoneal injection five times,
631 with 48-hour intervals between doses. Mice were monitored for at least one week before
632 the experiments commenced. For juvenile mice, 20 μg of tamoxifen dissolved in
633 sunflower oil was administered via intragastric injection at P3-5.

634 *Histology*

635 Mice were anesthetized with isoflurane, perfused using 4% paraformaldehyde (PFA),
636 and decapitated. Brains were post-fixed by 4% PFA overnight and then coronally
637 sectioned at 50 μm using a vibratome (VT-1000, Leica). For immunostaining, slices
638 were incubated in PBS-T (0.2% triton-X in PBS) containing 5% normal goat serum
639 (NGS) at room temperature for 1 h. Slices were then incubated with primary antibodies
640 of rabbit anti-Iba1 antibody (1:1000, #019-19741, Fujifilm) in PBS-T containing 5% NGS
641 for 48 h at 4°C. After washing with PBS-T, slices were incubated with secondary
642 antibodies conjugated with Alexa 488 or Alexa 594 (goat anti-rabbit IgG antibody, 1:500,
643 A-11008 or A-11012, Thermo Fisher Scientific) for 2 h at room temperature. For nuclear
644 staining, TO-PRO-3 (1:2000, T3605, Thermo Fisher Scientific) was incubated
645 simultaneously with the secondary antibodies. The slices were mounted in antifade
646 reagents (H-1000, Vectashield, Vector Laboratories). The slices were subjected to
647 imaging by confocal microscopy (TCS−SP5, Leica) or fluorescent microscopy with
648 structured illumination (BZX-810, Keyence).

649 Contours were traced by referring to the Allen Mouse Brain Atlas
650 (https://mouse.brain-map.org/static/atlas).

651 *Data analysis*

652 For spine volume analysis, three-dimensional reconstructions of dendritic morphology
653 were generated by the summation of z-stacked images separated by 0.5 μm. The

654 fluorescence intensity of dendritic spines was normalized by the entire fluorescence of
655 an imaging area. Spine-head volumes were estimated from the total fluorescence
656 intensity. Neighboring spines were defined as spines within 3 μm of the stimulated
657 spines. The baseline value for spine volume was calculated as the mean of the spine
658 volumes at 3 time points before uncaging. To calculate volume change, the baseline
659 was subtracted from the spine volume at each time point. Averaged volume changes at
660 40 and 50 minutes after STDP stimulation were calculated and were further averaged
661 over spines in the same dendrite for statistical analyses.

662 For microglia contact analysis, microglial morphology was assessed by summing
663 z-stacked images taken at 1 μm intervals across 5 slices, centered on the plane of
664 maximal intensity for each dendritic spine. At each time point, the presence of microglial
665 processes was recorded if the average signal within a region of interest (ROI) with a 4
666 μm diameter around the stimulated spine exceeded 3 standard deviations above the
667 background signal of a nearby area.

668 For image analysis in behavioral experiments assessing the spread of AIP expression
669 or microglial ablation, z-stacked images were processed with a Gaussian filter, and
670 autofluorescence signals from the neocortex were subtracted. Images from all mice
671 were subsequently registered and averaged. For the analysis of AIP expression, the
672 images were binarized prior to averaging. In the AIP experiment for observational fear
673 learning, two mice exhibiting no AIP expression and two mice with the center of AIP

674 expression deviating 0.6 mm anterior to the target were excluded from the analyses. No
675 mice were excluded in the microglial ablation experiment.

676 For freezing analysis from behavioral data, mouse morphology was detected in each
677 video frame using custom-written scripts with OpenCV in Python. Frame-by-frame
678 differences were then calculated and thresholded to identify freezing responses.

679 For photometry data, signals from 470 nm and 405 nm excitation were subtracted from
680 autofluorescent reference values. The signal was median-filtered and down-sampled to
681 2 Hz. Ratio of signal was calculated for each session.

682 For thermal preference analysis from behavioral data, mouse location was annotated in
683 each video frame using napari in Python. Frame ratios for occupying the lower
684 temperature chamber were then calculated.

685 *Statistical tests*

686 We used the Kruskal–Wallis test with post hoc Steel's test or Wilcoxon signed-rank test
687 with Bonferroni correction after Friedman test for multiple comparisons, the
688 Mann–Whitney U test, or the Wilcoxon signed-rank test, depending on the experimental
689 design. Results were considered significant if $P < 0.05$ in two-sided tests. Sample sizes
690 were determined based on previous experiments [33,34].

691

References

1. Feldman, D.E. (2009). Synaptic mechanisms for plasticity in neocortex. Annu. Rev. Neurosci. *32*, 33–55. 10.1146/annurev.neuro.051508.135516.

2. Buonomano, D.V., and Merzenich, M.M. (1998). Cortical plasticity: from synapses to maps. Annu. Rev. Neurosci. *21*, 149–186. 10.1146/annurev.neuro.21.1.149.

3. McClelland, J.L., McNaughton, B.L., and O'Reilly, R.C. (1995). Why there are complementary learning systems in the hippocampus and neocortex: Insights from the successes and failures of connectionist models of learning and memory. Psychol. Rev. *102*, 419–457. 10.1037/0033-295X.102.3.419.

4. Benna, M.K., and Fusi, S. (2016). Computational principles of synaptic memory consolidation. Nat. Neurosci. *19*, 1697–1706. 10.1038/nn.4401.

5. Kirkwood, A., Lee, H.K., and Bear, M.F. (1995). Co-regulation of long-term potentiation and experience-dependent synaptic plasticity in visual cortex by age and experience. Nature *375*, 328–331. 10.1038/375328a0.

6. Teyler, T.J., Perkins, A.T., and Harris, K.M. (1989). The development of long-term potentiation in hippocampus and neocortex. Neuropsychologia *27*, 31–39. 10.1016/0028-3932(89)90088-2.

7. Edagawa, Y., Saito, H., and Abe, K. (2001). Endogenous serotonin contributes to a developmental decrease in long-term potentiation in the rat visual cortex. J. Neurosci. *21*, 1532–1537. 10.1523/JNEUROSCI.21-05-01532.2001.

8. Yoshimura, Y., Ohmura, T., and Komatsu, Y. (2003). Two forms of synaptic plasticity with distinct dependence on age, experience, and NMDA receptor subtype in rat visual cortex. J. Neurosci. *23*, 6557–6566. 10.1523/JNEUROSCI.23-16-06557.2003.

9. Jiang, B., Treviño, M., and Kirkwood, A. (2007). Sequential development of long-term potentiation and depression in different layers of the mouse visual cortex. J. Neurosci. *27*, 9648–9652. 10.1523/JNEUROSCI.2655-07.2007.

10. Kitamura, T., Ogawa, S.K., Roy, D.S., Okuyama, T., Morrissey, M.D., Smith, L.M., Redondo, R.L., and Tonegawa, S. (2017). Engrams and circuits crucial for systems consolidation of a memory. Science *356*, 73–78. 10.1126/science.aam6808.

11. Silverstein, S.E., O'Sullivan, R., Bukalo, O., Pati, D., Schaffer, J.A., Limoges, A., Zsembik, L., Yoshida, T., O'Malley, J.J., Paletzki, R.F., et al. (2024). A distinct cortical code for socially learned threat. Nature *626*, 1066–1072. 10.1038/s41586-023-07008-1.

12. Loureiro, M., Achargui, R., Flakowski, J., Van Zessen, R., Stefanelli, T., Pascoli, V., and Lüscher, C. (2019). Social transmission of food safety depends on synaptic plasticity in the prefrontal cortex. Science *364*, 991–995. 10.1126/science.aaw5842.

13. Yashiro, K., and Philpot, B.D. (2008). Regulation of NMDA receptor subunit expression and its implications for LTD, LTP, and metaplasticity. Neuropharmacology *55*, 1081–1094. 10.1016/j.neuropharm.2008.07.046.

14. Lohmann, C., and Kessels, H.W. (2014). The developmental stages of synaptic plasticity. J Physiol (Lond) *592*, 13–31. 10.1113/jphysiol.2012.235119.

15. Hammond, T.R., Robinton, D., and Stevens, B. (2018). Microglia and the brain: complementary partners in development and disease. Annu. Rev. Cell Dev. Biol. *34*, 523–544. 10.1146/annurev-cellbio-100616-060509.

16. Parkhurst, C.N., Yang, G., Ninan, I., Savas, J.N., Yates, J.R., Lafaille, J.J., Hempstead, B.L., Littman, D.R., and Gan, W.-B. (2013). Microglia promote learning-dependent synapse formation through brain-derived neurotrophic factor. Cell *155*, 1596–1609. 10.1016/j.cell.2013.11.030.

17. Zhou, H.-C., Sun, Y.-Y., Cai, W., He, X.-T., Yi, F., Li, B.-M., and Zhang, X.-H. (2013). Activation of β2-adrenoceptor enhances synaptic potentiation and behavioral memory via cAMP-PKA signaling in the medial prefrontal cortex of rats. Learn. Mem. *20*, 274–284. 10.1101/lm.030411.113.

18. Seol, G.H., Ziburkus, J., Huang, S., Song, L., Kim, I.T., Takamiya, K., Huganir, R.L., Lee, H.-K., and Kirkwood, A. (2007). Neuromodulators control the polarity of spike-timing-dependent synaptic plasticity. Neuron *55*, 919–929. 10.1016/j.neuron.2007.08.013.

19. Flores, O., Pérez, H., Valladares, L., Morgan, C., Gatica, A., Burgos, H., Olivares, R., and Hernández, A. (2011). Hidden prenatal malnutrition in the rat: role of β_1-adrenoceptors on synaptic plasticity in the frontal cortex. J. Neurochem. *119*, 314–323. 10.1111/j.1471-4159.2011.07429.x.

20. Sáez-Briones, P., Soto-Moyano, R., Burgos, H., Castillo, A., Valladares, L., Morgan, C., Pérez, H., Barra, R., Constandil, L., Laurido, C., et al. (2015). β2-adrenoceptor stimulation restores frontal cortex plasticity and improves visuospatial performance in hidden-prenatally-malnourished young-adult rats. Neurobiol. Learn. Mem. *119*, 1–9. 10.1016/j.nlm.2014.11.003.

21. Pettigrew, J.D., and Kasamatsu, T. (1978). Local perfusion of noradrenaline maintains visual cortical plasticity. Nature *271*, 761–763. 10.1038/271761a0.

22. Anlezark, G.M., Crow, T.J., and Greenway, A.P. (1973). Impaired learning and decreased cortical norepinephrine after bilateral locus coeruleus lesions. Science *181*, 682–684. 10.1126/science.181.4100.682.

23. Uematsu, A., Tan, B.Z., Ycu, E.A., Cuevas, J.S., Koivumaa, J., Junyent, F., Kremer, E.J., Witten, I.B., Deisseroth, K., and Johansen, J.P. (2017). Modular organization of the brainstem noradrenaline system coordinates opposing learning states. Nat. Neurosci. *20*, 1602–1611. 10.1038/nn.4642.

24. Stowell, R.D., Sipe, G.O., Dawes, R.P., Batchelor, H.N., Lordy, K.A., Whitelaw, B.S., Stoessel, M.B., Bidlack, J.M., Brown, E., Sur, M., et al. (2019). Noradrenergic signaling in the wakeful state inhibits microglial surveillance and synaptic plasticity in the mouse visual cortex. Nat. Neurosci. *22*, 1782–1792. 10.1038/s41593-019-0514-0.

25. Liu, Y.U., Ying, Y., Li, Y., Eyo, U.B., Chen, T., Zheng, J., Umpierre, A.D., Zhu, J., Bosco, D.B., Dong, H., et al. (2019). Neuronal network activity controls microglial process surveillance in awake mice via norepinephrine signaling. Nat. Neurosci. *22*, 1771–1781. 10.1038/s41593-019-0511-3.

26. Herring, B.E., and Nicoll, R.A. (2016). Long-Term Potentiation: From CaMKII to AMPA Receptor Trafficking. Annu. Rev. Physiol. *78*, 351–365. 10.1146/annurev-physiol-021014-071753.

27. Kasai, H., Ziv, N.E., Okazaki, H., Yagishita, S., and Toyoizumi, T. (2021). Spine dynamics in the brain, mental disorders and artificial neural networks. Nat. Rev. Neurosci. *22*, 407–422. 10.1038/s41583-021-00467-3.

28. Matsuzaki, M., Honkura, N., Ellis-Davies, G.C.R., and Kasai, H. (2004). Structural basis of long-term potentiation in single dendritic spines. Nature *429*, 761–766. 10.1038/nature02617.

29. Harvey, C.D., Yasuda, R., Zhong, H., and Svoboda, K. (2008). The spread of Ras activity triggered by activation of a single dendritic spine. Science *321*, 136–140. 10.1126/science.1159675.

30. Bosch, M., Castro, J., Saneyoshi, T., Matsuno, H., Sur, M., and Hayashi, Y. (2014). Structural and molecular remodeling of dendritic spine substructures during long-term potentiation. Neuron *82*, 444–459. 10.1016/j.neuron.2014.03.021.

31. Ji, K., Akgul, G., Wollmuth, L.P., and Tsirka, S.E. (2013). Microglia actively regulate the number of functional synapses. PLoS ONE *8*, e56293. 10.1371/journal.pone.0056293.

32. Kaiser, T., and Feng, G. (2019). Tmem119-EGFP and Tmem119-CreERT2

797 Transgenic Mice for Labeling and Manipulating Microglia. eNeuro *6*.
798 10.1523/ENEURO.0448-18.2019.

799 33. Iino, Y., Sawada, T., Yamaguchi, K., Tajiri, M., Ishii, S., Kasai, H., and Yagishita, S.
800 (2020). Dopamine D2 receptors in discrimination learning and spine enlargement.
801 Nature *579*, 555–560. 10.1038/s41586-020-2115-1.

802 34. Yagishita, S., Hayashi-Takagi, A., Ellis-Davies, G.C.R., Urakubo, H., Ishii, S., and
803 Kasai, H. (2014). A critical time window for dopamine actions on the structural
804 plasticity of dendritic spines. Science *345*, 1616–1620. 10.1126/science.1255514.

805 35. Jin, W.-N., Shi, S.X.-Y., Li, Z., Li, M., Wood, K., Gonzales, R.J., and Liu, Q. (2017).
806 Depletion of microglia exacerbates postischemic inflammation and brain injury. J.
807 Cereb. Blood Flow Metab. *37*, 2224–2236. 10.1177/0271678X17694185.

808 36. Noguchi, J., Nagaoka, A., Watanabe, S., Ellis-Davies, G.C.R., Kitamura, K., Kano,
809 M., Matsuzaki, M., and Kasai, H. (2011). In vivo two-photon uncaging of glutamate
810 revealing the structure-function relationships of dendritic spines in the neocortex of
811 adult mice. J Physiol (Lond) *589*, 2447–2457. 10.1113/jphysiol.2011.207100.

812 37. Holler, S., Köstinger, G., Martin, K.A.C., Schuhknecht, G.F.P., and Stratford, K.J.
813 (2021). Structure and function of a neocortical synapse. Nature *591*, 111–116.
814 10.1038/s41586-020-03134-2.

815 38. Berki, P., Cserép, C., Környei, Z., Pósfai, B., Szabadits, E., Domonkos, A.,
816 Kellermayer, A., Nyerges, M., Wei, X., Mody, I., et al. (2024). Microglia contribute
817 to neuronal synchrony despite endogenous ATP-related phenotypic transformation
818 in acute mouse brain slices. Nat. Commun. *15*, 5402.
819 10.1038/s41467-024-49773-1.

820 39. Tremblay, M.-È., Lowery, R.L., and Majewska, A.K. (2010). Microglial interactions
821 with synapses are modulated by visual experience. PLoS Biol. *8*, e1000527.
822 10.1371/journal.pbio.1000527.

823 40. Escoubas, C.C., and Molofsky, A.V. (2024). Microglia as integrators of
824 brain-associated molecular patterns. Trends Immunol. *45*, 358–370.
825 10.1016/j.it.2024.03.009.

826 41. Cornell, J., Salinas, S., Huang, H.-Y., and Zhou, M. (2022). Microglia regulation of
827 synaptic plasticity and learning and memory. Neural Regen. Res. *17*, 705–716.
828 10.4103/1673-5374.322423.

829 42. Ren, S., Yao, W., Tambini, M.D., Yin, T., Norris, K.A., and D'Adamio, L. (2020).
830 Microglia TREM2R47H Alzheimer-linked variant enhances excitatory transmission
831 and reduces LTP via increased TNF-α levels. eLife *9*. 10.7554/eLife.57513.

43. Hoshino, K., Hasegawa, K., Kamiya, H., and Morimoto, Y. (2017). Synapse-specific effects of IL-1β on long-term potentiation in the mouse hippocampus. Biomed. Res. *38*, 183–188. 10.2220/biomedres.38.183.

44. Rogers, J.T., Morganti, J.M., Bachstetter, A.D., Hudson, C.E., Peters, M.M., Grimmig, B.A., Weeber, E.J., Bickford, P.C., and Gemma, C. (2011). CX3CR1 deficiency leads to impairment of hippocampal cognitive function and synaptic plasticity. J. Neurosci. *31*, 16241–16250. 10.1523/JNEUROSCI.3667-11.2011.

45. Liu, T., Lu, J., Lukasiewicz, K., Pan, B., and Zuo, Y. (2021). Stress induces microglia-associated synaptic circuit alterations in the dorsomedial prefrontal cortex. Neurobiol. Stress, 100342. 10.1016/j.ynstr.2021.100342.

46. Weinhard, L., di Bartolomei, G., Bolasco, G., Machado, P., Schieber, N.L., Neniskyte, U., Exiga, M., Vadisiute, A., Raggioli, A., Schertel, A., et al. (2018). Microglia remodel synapses by presynaptic trogocytosis and spine head filopodia induction. Nat. Commun. *9*, 1228. 10.1038/s41467-018-03566-5.

47. Wake, H., Moorhouse, A.J., Jinno, S., Kohsaka, S., and Nabekura, J. (2009). Resting microglia directly monitor the functional state of synapses in vivo and determine the fate of ischemic terminals. J. Neurosci. *29*, 3974–3980. 10.1523/JNEUROSCI.4363-08.2009.

48. Miyamoto, A., Wake, H., Ishikawa, A.W., Eto, K., Shibata, K., Murakoshi, H., Koizumi, S., Moorhouse, A.J., Yoshimura, Y., and Nabekura, J. (2016). Microglia contact induces synapse formation in developing somatosensory cortex. Nat. Commun. *7*, 12540. 10.1038/ncomms12540.

49. Haynes, S.E., Hollopeter, G., Yang, G., Kurpius, D., Dailey, M.E., Gan, W.-B., and Julius, D. (2006). The P2Y12 receptor regulates microglial activation by extracellular nucleotides. Nat. Neurosci. *9*, 1512–1519. 10.1038/nn1805.

50. Tasic, B., Yao, Z., Graybuck, L.T., Smith, K.A., Nguyen, T.N., Bertagnolli, D., Goldy, J., Garren, E., Economo, M.N., Viswanathan, S., et al. (2018). Shared and distinct transcriptomic cell types across neocortical areas. Nature *563*, 72–78. 10.1038/s41586-018-0654-5.

51. Davies, C.A., Loddick, S.A., Toulmond, S., Stroemer, R.P., Hunt, J., and Rothwell, N.J. (1999). The progression and topographic distribution of interleukin-1beta expression after permanent middle cerebral artery occlusion in the rat. J. Cereb. Blood Flow Metab. *19*, 87–98. 10.1097/00004647-199901000-00010.

52. Nie, X., Kitaoka, S., Tanaka, K., Segi-Nishida, E., Imoto, Y., Ogawa, A., Nakano, F., Tomohiro, A., Nakayama, K., Taniguchi, M., et al. (2018). The Innate Immune Receptors TLR2/4 Mediate Repeated Social Defeat Stress-Induced Social

Avoidance through Prefrontal Microglial Activation. Neuron *99*, 464-479.e7. 10.1016/j.neuron.2018.06.035.

53. Zhang, Y., Chen, K., Sloan, S.A., Bennett, M.L., Scholze, A.R., O'Keeffe, S., Phatnani, H.P., Guarnieri, P., Caneda, C., Ruderisch, N., et al. (2014). An RNA-sequencing transcriptome and splicing database of glia, neurons, and vascular cells of the cerebral cortex. J. Neurosci. *34*, 11929–11947. 10.1523/JNEUROSCI.1860-14.2014.

54. Elmore, M.R.P., Najafi, A.R., Koike, M.A., Dagher, N.N., Spangenberg, E.E., Rice, R.A., Kitazawa, M., Matusow, B., Nguyen, H., West, B.L., et al. (2014). Colony-stimulating factor 1 receptor signaling is necessary for microglia viability, unmasking a microglia progenitor cell in the adult brain. Neuron *82*, 380–397. 10.1016/j.neuron.2014.02.040.

55. Beattie, E.C., Stellwagen, D., Morishita, W., Bresnahan, J.C., Ha, B.K., Von Zastrow, M., Beattie, M.S., and Malenka, R.C. (2002). Control of synaptic strength by glial TNFalpha. Science *295*, 2282–2285. 10.1126/science.1067859.

56. Parameswaran, N., and Patial, S. (2010). Tumor necrosis factor-α signaling in macrophages. Crit. Rev. Eukaryot. Gene Expr. *20*, 87–103. 10.1615/critreveukargeneexpr.v20.i2.10.

57. Zunke, F., and Rose-John, S. (2017). The shedding protease ADAM17: Physiology and pathophysiology. Biochim. Biophys. Acta Mol. Cell Res. *1864*, 2059–2070. 10.1016/j.bbamcr.2017.07.001.

58. Wang, J.-Y., Huang, Y.-N., Chiu, C.-C., Tweedie, D., Luo, W., Pick, C.G., Chou, S.-Y., Luo, Y., Hoffer, B.J., Greig, N.H., et al. (2016). Pomalidomide mitigates neuronal loss, neuroinflammation, and behavioral impairments induced by traumatic brain injury in rat. J. Neuroinflammation *13*, 168. 10.1186/s12974-016-0631-6.

59. Shortt, J., Hsu, A.K., and Johnstone, R.W. (2013). Thalidomide-analogue biology: immunological, molecular and epigenetic targets in cancer therapy. Oncogene *32*, 4191–4202. 10.1038/onc.2012.599.

60. Masuda, T., Sankowski, R., Staszewski, O., Böttcher, C., Amann, L., Sagar, Scheiwe, C., Nessler, S., Kunz, P., van Loo, G., et al. (2019). Spatial and temporal heterogeneity of mouse and human microglia at single-cell resolution. Nature *566*, 388–392. 10.1038/s41586-019-0924-x.

61. Kim, J.-H., Choi, D.-E., and Shin, H.-S. (2025). The lateralized LC-NAergic system distinguishes vicarious versus direct fear in mice. Nat. Commun. *16*, 2364.

903 10.1038/s41467-025-57701-0.

904 62. Guo, L., Xiong, H., Kim, J.-I., Wu, Y.-W., Lalchandani, R.R., Cui, Y., Shu, Y., Xu, T.,
905 and Ding, J.B. (2015). Dynamic rewiring of neural circuits in the motor cortex in
906 mouse models of Parkinson's disease. Nat. Neurosci. *18*, 1299–1309.
907 10.1038/nn.4082.

908 63. Hu, H., Real, E., Takamiya, K., Kang, M.-G., Ledoux, J., Huganir, R.L., and
909 Malinow, R. (2007). Emotion enhances learning via norepinephrine regulation of
910 AMPA-receptor trafficking. Cell *131*, 160–173. 10.1016/j.cell.2007.09.017.

911 64. Winder, D.G., Martin, K.C., Muzzio, I.A., Rohrer, D., Chruscinski, A., Kobilka, B.,
912 and Kandel, E.R. (1999). ERK plays a regulatory role in induction of LTP by theta
913 frequency stimulation and its modulation by beta-adrenergic receptors. Neuron *24*,
914 715–726. 10.1016/s0896-6273(00)81124-1.

915 65. Murugan, M., Jang, H.J., Park, M., Miller, E.M., Cox, J., Taliaferro, J.P., Parker,
916 N.F., Bhave, V., Hur, H., Liang, Y., et al. (2017). Combined Social and Spatial
917 Coding in a Descending Projection from the Prefrontal Cortex. Cell *171*,
918 1663-1677.e16. 10.1016/j.cell.2017.11.002.

919 66. Bernier, L.-P., Bohlen, C.J., York, E.M., Choi, H.B., Kamyabi, A., Dissing-Olesen,
920 L., Hefendehl, J.K., Collins, H.Y., Stevens, B., Barres, B.A., et al. (2019).
921 Nanoscale Surveillance of the Brain by Microglia via cAMP-Regulated Filopodia.
922 Cell Rep. *27*, 2895-2908.e4. 10.1016/j.celrep.2019.05.010.

923 67. Vecsey, C.G., Baillie, G.S., Jaganath, D., Havekes, R., Daniels, A., Wimmer, M.,
924 Huang, T., Brown, K.M., Li, X.-Y., Descalzi, G., et al. (2009). Sleep deprivation
925 impairs cAMP signalling in the hippocampus. Nature *461*, 1122–1125.
926 10.1038/nature08488.

927 68. Yamaguchi, K., Maeda, Y., Sawada, T., Iino, Y., Tajiri, M., Nakazato, R., Ishii, S.,
928 Kasai, H., and Yagishita, S. (2022). A behavioural correlate of the synaptic
929 eligibility trace in the nucleus accumbens. Sci. Rep. *12*, 1921.
930 10.1038/s41598-022-05637-6.

931 69. Tanaka, J.-I., Horiike, Y., Matsuzaki, M., Miyazaki, T., Ellis-Davies, G.C.R., and
932 Kasai, H. (2008). Protein synthesis and neurotrophin-dependent structural
933 plasticity of single dendritic spines. Science *319*, 1683–1687.
934 10.1126/science.1152864.

935 70. Zhu, H., Aryal, D.K., Olsen, R.H.J., Urban, D.J., Swearingen, A., Forbes, S., Roth,
936 B.L., and Hochgeschwender, U. (2016). Cre-dependent DREADD (Designer
937 Receptors Exclusively Activated by Designer Drugs) mice. Genesis *54*, 439–446.

938 10.1002/dvg.22949.

939 71. Ma, C., Li, B., Silverman, D., Ding, X., Li, A., Xiao, C., Huang, G., Worden, K.,
940 Muroy, S., Chen, W., et al. (2024). Microglia regulate sleep through
941 calcium-dependent modulation of norepinephrine transmission. Nat. Neurosci. *27*,
942 249–258. 10.1038/s41593-023-01548-5.

943 72. Nagai, Y., Miyakawa, N., Takuwa, H., Hori, Y., Oyama, K., Ji, B., Takahashi, M.,
944 Huang, X.-P., Slocum, S.T., DiBerto, J.F., et al. (2020). Deschloroclozapine, a
945 potent and selective chemogenetic actuator enables rapid neuronal and
946 behavioral modulations in mice and monkeys. Nat. Neurosci. *23*, 1157–1167.
947 10.1038/s41593-020-0661-3.

948 73. Yun, S., Yang, B., Anair, J.D., Martin, M.M., Fleps, S.W., Pamukcu, A., Yeh, N.-H.,
949 Contractor, A., Kennedy, A., and Parker, J.G. (2023). Antipsychotic drug efficacy
950 correlates with the modulation of D1 rather than D2 receptor-expressing striatal
951 projection neurons. Nat. Neurosci. *26*, 1417–1428. 10.1038/s41593-023-01390-9.

952 74. Han, K.A., Yoon, T.-H., Kim, J., Lee, J., Lee, J.Y., Jang, G., Um, J.W., Kim, J.K.,
953 and Ko, J. (2024). Specification of neural circuit architecture shaped by
954 context-dependent patterned LAR-RPTP microexons. Nat. Commun. *15*, 1624.
955 10.1038/s41467-024-45695-0.

956 75. Allsop, S.A., Wichmann, R., Mills, F., Burgos-Robles, A., Chang, C.-J., Felix-Ortiz,
957 A.C., Vienne, A., Beyeler, A., Izadmehr, E.M., Glober, G., et al. (2018).
958 Corticoamygdala transfer of socially derived information gates observational
959 learning. Cell *173*, 1329-1342.e18. 10.1016/j.cell.2018.04.004.

960 76. Jeon, D., Kim, S., Chetana, M., Jo, D., Ruley, H.E., Lin, S.-Y., Rabah, D., Kinet,
961 J.-P., and Shin, H.-S. (2010). Observational fear learning involves affective pain
962 system and Cav1.2 Ca2+ channels in ACC. Nat. Neurosci. *13*, 482–488.
963 10.1038/nn.2504.

964 77. Olsson, A., Knapska, E., and Lindström, B. (2020). The neural and computational
965 systems of social learning. Nat. Rev. Neurosci. *21*, 197–212.
966 10.1038/s41583-020-0276-4.

967 78. Feng, J., Dong, H., Lischinsky, J.E., Zhou, J., Deng, F., Zhuang, C., Miao, X.,
968 Wang, H., Li, G., Cai, R., et al. (2024). Monitoring norepinephrine release in vivo
969 using next-generation GRABNE sensors. Neuron *112*, 1930-1942.e6.
970 10.1016/j.neuron.2024.03.001.

971 79. Basu, A., Yang, J.-H., Yu, A., Glaeser-Khan, S., Rondeau, J.A., Feng, J., Krystal,
972 J.H., Li, Y., and Kaye, A.P. (2024). Frontal norepinephrine represents a threat
973 prediction error under uncertainty. Biol. Psychiatry *96*, 256–267.

10.1016/j.biopsych.2024.01.025.

80. Terranova, J.I., Yokose, J., Osanai, H., Ogawa, S.K., and Kitamura, T. (2023). Systems consolidation induces multiple memory engrams for a flexible recall strategy in observational fear memory in male mice. Nat. Commun. *14*, 3976. 10.1038/s41467-023-39718-5.

81. Zhuo, M. (2008). Cortical excitation and chronic pain. Trends Neurosci. *31*, 199–207. 10.1016/j.tins.2008.01.003.

82. Bliss, T.V.P., Collingridge, G.L., Kaang, B.-K., and Zhuo, M. (2016). Synaptic plasticity in the anterior cingulate cortex in acute and chronic pain. Nat. Rev. Neurosci. *17*, 485–496. 10.1038/nrn.2016.68.

83. Choi, J., Lee, Y.-B., So, D., Kim, J.Y., Choi, S., Kim, S., and Keum, S. (2025). Cortical representations of affective pain shape empathic fear in male mice. Nat. Commun. *16*, 1937. 10.1038/s41467-025-57230-w.

84. Smith, M.L., Asada, N., and Malenka, R.C. (2021). Anterior cingulate inputs to nucleus accumbens control the social transfer of pain and analgesia. Science *371*, 153–159. 10.1126/science.abe3040.

85. Hensch, T.K. (2004). Critical period regulation. Annu. Rev. Neurosci. *27*, 549–579. 10.1146/annurev.neuro.27.070203.144327.

86. He, K., Huertas, M., Hong, S.Z., Tie, X., Hell, J.W., Shouval, H., and Kirkwood, A. (2015). Distinct eligibility traces for LTP and LTD in cortical synapses. Neuron *88*, 528–538. 10.1016/j.neuron.2015.09.037.

87. Inaba, M., Maruyama, T., Yoshimura, Y., Hosoi, H., and Komatsu, Y. (2009). Facilitation of low-frequency stimulation-induced long-term potentiation by endogenous noradrenaline and serotonin in developing rat visual cortex. Neurosci. Res. *64*, 191–198. 10.1016/j.neures.2009.02.014.

88. Abel, T., Nguyen, P.V., Barad, M., Deuel, T.A., Kandel, E.R., and Bourtchouladze, R. (1997). Genetic demonstration of a role for PKA in the late phase of LTP and in hippocampus-based long-term memory. Cell *88*, 615–626. 10.1016/s0092-8674(00)81904-2.

89. Govindarajan, A., Israely, I., Huang, S.-Y., and Tonegawa, S. (2011). The dendritic branch is the preferred integrative unit for protein synthesis-dependent LTP. Neuron *69*, 132–146. 10.1016/j.neuron.2010.12.008.

90. Guirao, X., Kumar, A., Katz, J., Smith, M., Lin, E., Keogh, C., Calvano, S.E., and Lowry, S.F. (1997). Catecholamines increase monocyte TNF receptors and inhibit TNF through beta 2-adrenoreceptor activation. Am. J. Physiol. *273*, E1203-8.

1009 10.1152/ajpendo.1997.273.6.E1203.

1010 91. Ağaç, D., Estrada, L.D., Maples, R., Hooper, L.V., and Farrar, J.D. (2018). The
1011 β2-adrenergic receptor controls inflammation by driving rapid IL-10 secretion.
1012 Brain Behav. Immun. *74*, 176–185. 10.1016/j.bbi.2018.09.004.

1013 92. Zinyama, R.B., Bancroft, G.J., and Sigola, L.B. (2001). Adrenaline suppression of
1014 the macrophage nitric oxide response to lipopolysaccharide is associated with
1015 differential regulation of tumour necrosis factor-alpha and interleukin-10.
1016 Immunology *104*, 439–446. 10.1046/j.1365-2567.2001.01332.x.

1017 93. Deng, J., Muthu, K., Gamelli, R., Shankar, R., and Jones, S.B. (2004). Adrenergic
1018 modulation of splenic macrophage cytokine release in polymicrobial sepsis. Am J
1019 Physiol, Cell Physiol *287*, C730-6. 10.1152/ajpcell.00562.2003.

1020 94. Tye, K.M., Miller, E.K., Taschbach, F.H., Benna, M.K., Rigotti, M., and Fusi, S.
1021 (2024). Mixed selectivity: Cellular computations for complexity. Neuron *112*,
1022 2289–2303. 10.1016/j.neuron.2024.04.017.

1023 95. El-Boustani, S., Ip, J.P.K., Breton-Provencher, V., Knott, G.W., Okuno, H., Bito, H.,
1024 and Sur, M. (2018). Locally coordinated synaptic plasticity of visual cortex neurons
1025 in vivo. Science *360*, 1349–1354. 10.1126/science.aao0862.

1026 96. Cichon, J., and Gan, W.-B. (2015). Branch-specific dendritic Ca(2+) spikes cause
1027 persistent synaptic plasticity. Nature *520*, 180–185. 10.1038/nature14251.

1028 97. Noguchi, J., Nagaoka, A., Hayama, T., Ucar, H., Yagishita, S., Takahashi, N., and
1029 Kasai, H. (2019). Bidirectional in vivo structural dendritic spine plasticity revealed
1030 by two-photon glutamate uncaging in the mouse neocortex. Sci. Rep. *9*, 13922.
1031 10.1038/s41598-019-50445-0.

1032 98. Tazerart, S., Mitchell, D.E., Miranda-Rottmann, S., and Araya, R. (2020). A
1033 spike-timing-dependent plasticity rule for dendritic spines. Nat. Commun. *11*, 4276.
1034 10.1038/s41467-020-17861-7.

1035 99. Basilico, B., Ferrucci, L., Ratano, P., Golia, M.T., Grimaldi, A., Rosito, M., Ferretti,
1036 V., Reverte, I., Sanchini, C., Marrone, M.C., et al. (2022). Microglia control
1037 glutamatergic synapses in the adult mouse hippocampus. Glia *70*, 173–195.
1038 10.1002/glia.24101.

1039 100. Nguyen, P.T., Dorman, L.C., Pan, S., Vainchtein, I.D., Han, R.T., Nakao-Inoue, H.,
1040 Taloma, S.E., Barron, J.J., Molofsky, A.B., Kheirbek, M.A., et al. (2020). Microglial
1041 remodeling of the extracellular matrix promotes synapse plasticity. Cell *182*,
1042 388-403.e15. 10.1016/j.cell.2020.05.050.

1043 101. Paus, T., Keshavan, M., and Giedd, J.N. (2008). Why do many psychiatric

1044 disorders emerge during adolescence? Nat. Rev. Neurosci. *9*, 947–957.
1045 10.1038/nrn2513.

1046 102. Mondelli, V., Vernon, A.C., Turkheimer, F., Dazzan, P., and Pariante, C.M. (2017).
1047 Brain microglia in psychiatric disorders. Lancet Psychiatry *4*, 563–572.
1048 10.1016/S2215-0366(17)30101-3.

1049 103. Grieger, J.C., Choi, V.W., and Samulski, R.J. (2006). Production and
1050 characterization of adeno-associated viral vectors. Nat. Protoc. *1*, 1412–1428.
1051 10.1038/nprot.2006.207.

Figures

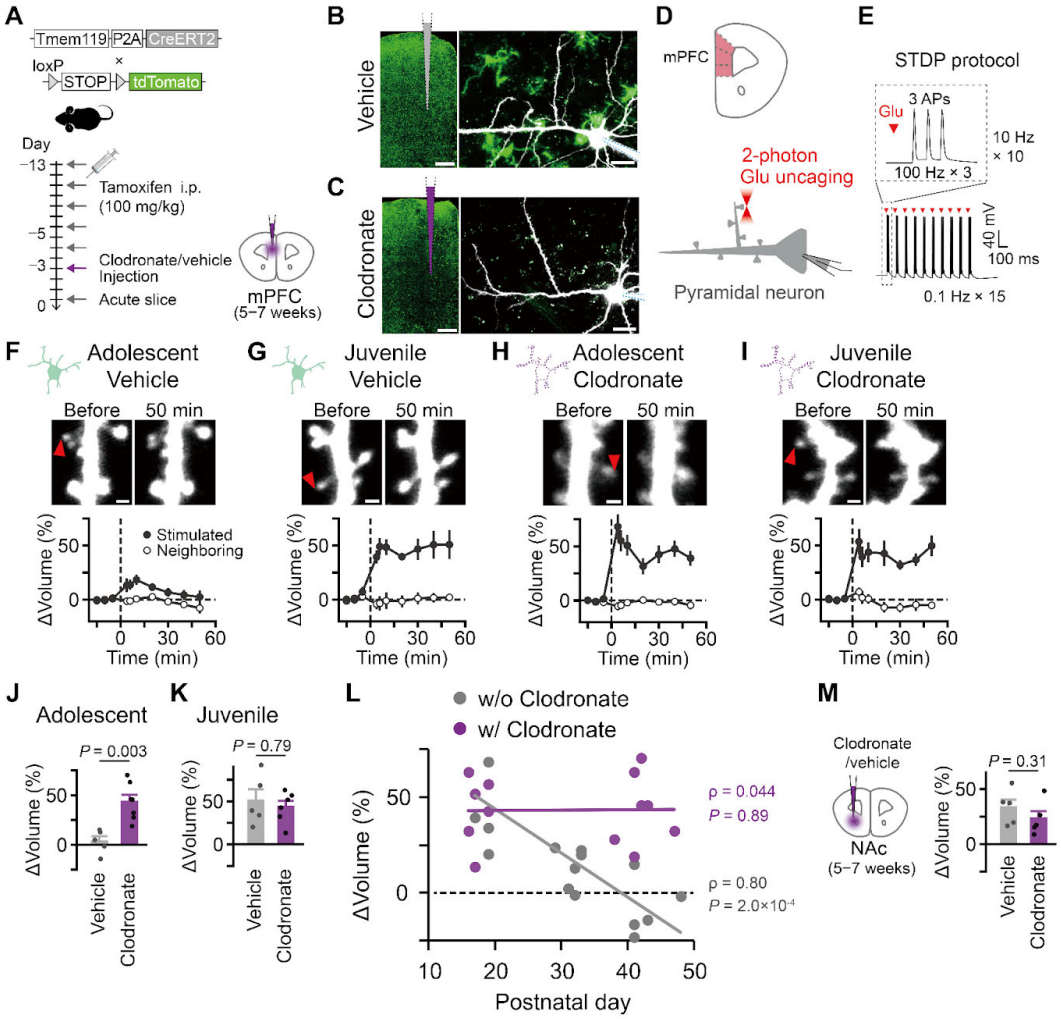

Figure 1. Microglial suppression of spine enlargement.
A, Schematic of a typical experimental timeline in adolescent (5–7 weeks old) transgenic mice.
B,C, Representative images of fixed slices with confocal microscopy (left) and acute slices with 2-photon microscopy after vehicle (B) or clodronate (C) injections. Fluorescences of tdTomato for microglia (green) and Alexa 488 for neurons (white) are shown. Dotted lines indicate injection traces. Scale bars, 500 μm (left) and 20 μm (right).

D, Schematic of a brain slice containing the mPFC (top) and the experimental configuration for two-photon uncaging on dendritic spines of a pyramidal neuron (bottom). Caged-glutamate (CDNI-Glutamate, 4 mM) was applied using a puff pipette. Glu, glutamate.
E, Schematic of the spike-timing-dependent plasticity (STDP) protocol. Each train consisted of 10 bursts (3 action potentials [APs] at 100 Hz) delivered at 10 Hz. The train was repeated 15 times at 0.1 Hz.
F–I, Representative images of dendritic spines before and 50 minutes after STDP stimulation (top) and time courses of spine volume changes (bottom) in juvenile mice (2−3 weeks old) (F,H) and the adolescent mice (G, I) after vehicle (F, G) or clodronate (H, I) injections. Red arrows indicate stimulated spines. Scale bars, 1 μm.
J,K, Plots of spine volume changes. Volume changes were averaged over 40−50 minutes.
L, Plots of spine volume changes across ages. Statistical analysis was performed using Spearman's rank correlation coefficient test.
M, Schematic of clodronate injection into the nucleus accumbens (NAc) in adolescent mice (5–7 weeks old) (left) and plots of spine volume changes (right).
Error bars represent S.E.M. Mann–Whitney U test used for statistical analysis in (J,K,M).

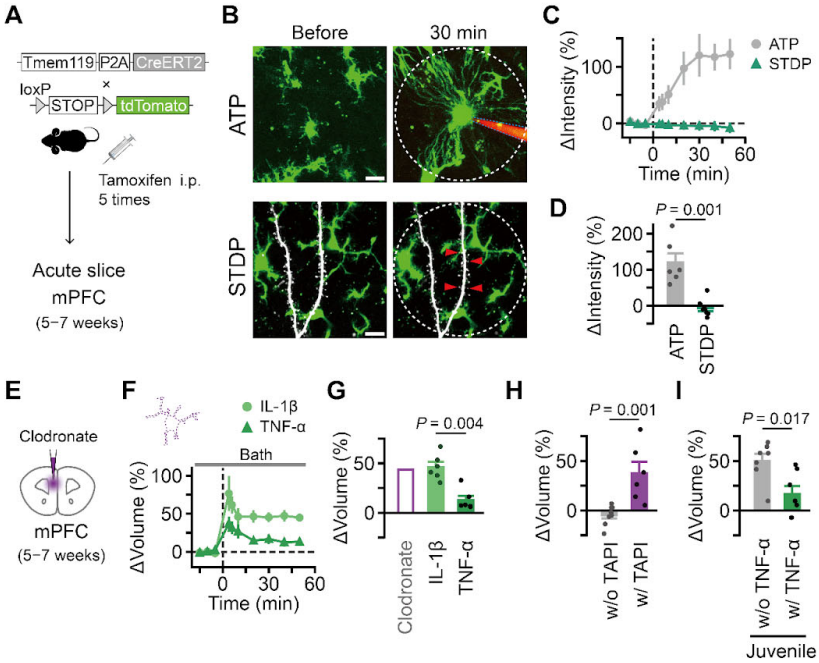

Figure 2. Signaling of microglial suppression.
A, Schematic of the experimental timeline.
B, Representative z-stack images (30 μm thick) of acute slices with 2-photon microscopy before (left) and after (right) ATP application from pipette (top) or STDP stimulation (bottom). Fluorescences of tdTomato for microglia (green), Alexa 488 for neurons (white), and Alexa 488 with 20 mM ATP in ACSF contained in the pipette (red) are shown. Red arrows indicate stimulated spines. White dotted circles denote the regions of interest (70 μm in diameter, centered at the ATP pipette tip or the stimulated spine area) for quantitative analyses. Scale bars, 10 μm.
C,D, Time courses (C) and plots (D) of changes in intensity in the regions of interest indicated in (B).
E, Schematic of clodronate injection.
F,G, Time courses (F) and plots (G) of spine volume changes in the slices with clodronate injections in the presence of IL-1β and TNF-α. The clodronate injection condition shown in (Figure 1J) is indicated as a reference.
H,I, Plots of spine volume changes following STDP stimulation in the absence and presence of TAPI-0 (TACE/ADAM17 inhibitor) (H) or in the absence and presence of TNF-α from juvenile mice (I). No clodronate injections were performed in these experiments.
Error bars represent S.E.M. Mann–Whitney U test used for statistical analysis in (D,G,H,I).

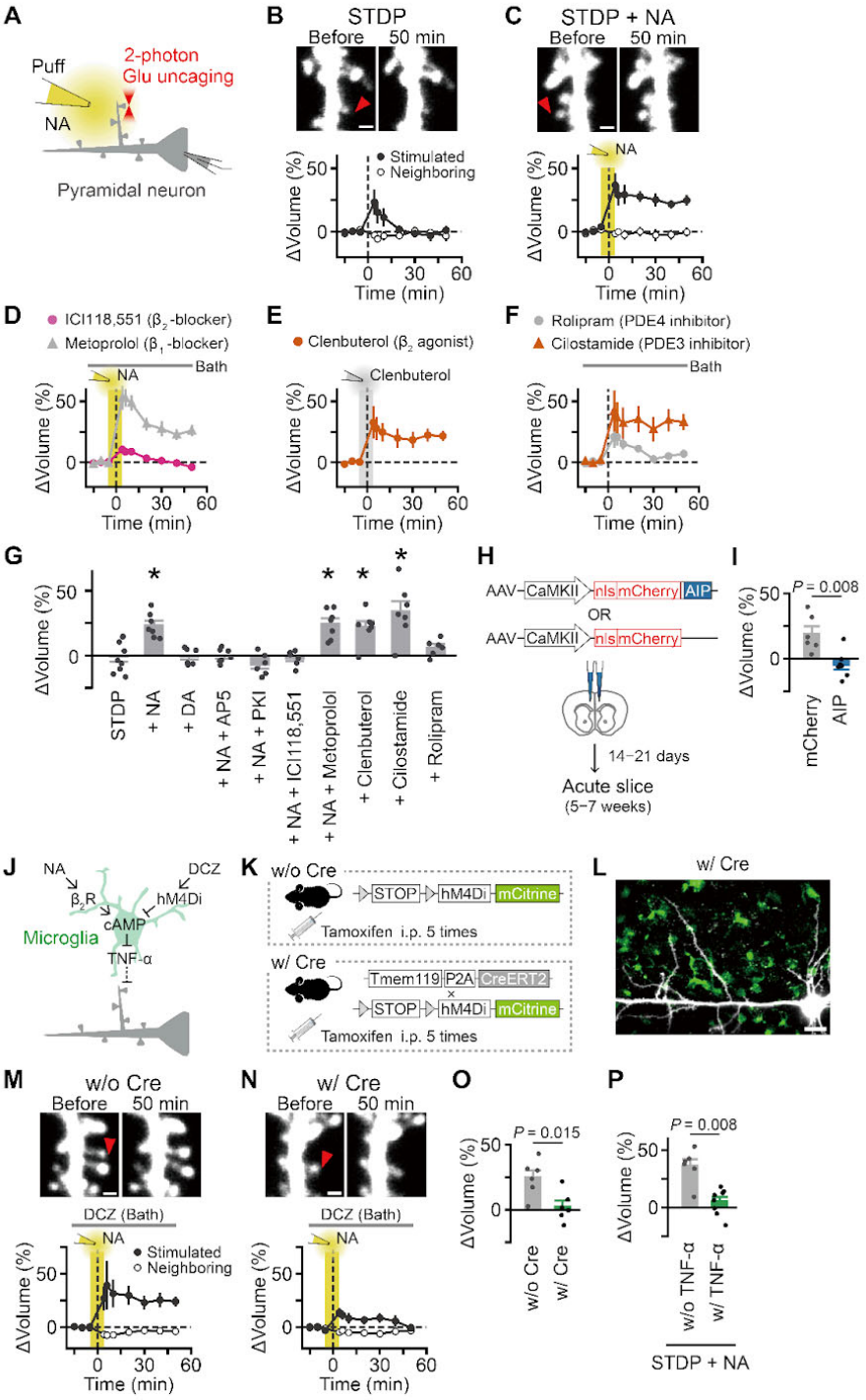
A
Puff
2-photon
Glu uncaging
NA
Pyramidal neuron
B
STDP
Before
50 min
Stimulated
Neighboring
ΔVolume (%)
Time (min)
C
STDP + NA
Before
50 min
NA
D
ICI118,551 (β2-blocker)
Metoprolol (β1-blocker)
Bath
E
Clenbuterol (β2 agonist)
Clenbuterol
F
Rolipram (PDE4 inhibitor)
Cilostamide (PDE3 inhibitor)
G
STDP
+ NA
+ DA
+ NA + AP5
+ NA + PKI
+ NA + ICI118,551
+ NA + Metoprolol
+ Clenbuterol
+ Cilostamide
+ Rolipram
H
AAV–CaMKII
nls mCherry
AIP
OR
14–21 days
Acute slice
(5–7 weeks)
I
P = 0.008
mCherry
AIP
J
NA
DCZ
β2R
hM4Di
cAMP
Microglia
TNF-α
K
w/o Cre
STOP
hM4Di
mCitrine
Tamoxifen i.p. 5 times
w/ Cre
Tmem119
P2A
CreERT2
L
w/ Cre
M
w/o Cre
DCZ (Bath)
N
w/ Cre
O
P = 0.015
w/o Cre
w/ Cre
P
P = 0.008
w/o TNF-α
w/ TNF-α
STDP + NA

Figure 3. Microglia-mediated noradrenaline actions on spine enlargement.
A, Schematic of the experimental configuration for puff application and two-photon uncaging on dendritic spines of a pyramidal neuron.
B,C, Representative images of dendritic spines before and 50 minutes after STDP stimulation (top) and time courses of spine volume changes after STDP stimulation (bottom) in the absence (B) and presence (C) of NA. Red arrows indicate stimulated spines. Shaded areas indicate the period of puff application. Scale bars, 1 μm.
D–F, Time courses of spine volume changes in the presence of β blockers with NA (D), β_2 agonist (E), and phosphodiesterase inhibitors (F). Gray shade and bars indicate the period of drug application.
G, Plots of spine volume changes. Volume changes were averaged over 40−50 minutes and subjected to statistical tests (Kruskal–Wallis test and post hoc Steel's test against STDP only). $^*P < 0.05$.
Error bars represent S.E.M.
H, Schematics of AAV vectors to express mCherry with or without AIP.
I, Plots of spine volume changes.
J, Schematic of a signaling model.
K, Schematic of R26-LSL-hM4Di-mCitrine mice without (w/o Cre) and with (w/ Cre) Tmem119-CreERT2 allele.
L, Image of an acute slice with 2-photon microscopy from a transgenic mouse (w/ Cre). Fluorescences of mCitrine (green) and Alexa 594 (white) are shown. Scale bar, 20 μm.
M,N, Representative images of dendritic spines before and 50 minutes after STDP stimulation (top) and time courses of spine volumes (bottom) in the slices without (M) and with (N) Cre. Gray bars indicate the period of DCZ (100 nM) application. Red arrows indicate stimulated spines. Scale bars, 1 μm.
O, Plots for spine volumes shown in (M,N).
P, Plots of spine volume changes in the absence and presence of TNF-α following STDP stimulation in the presence of NA from Supplementary Figure 6G.
Error bars represent S.E.M. Statistical analysis was performed using the Mann–Whitney U test in (F,G).

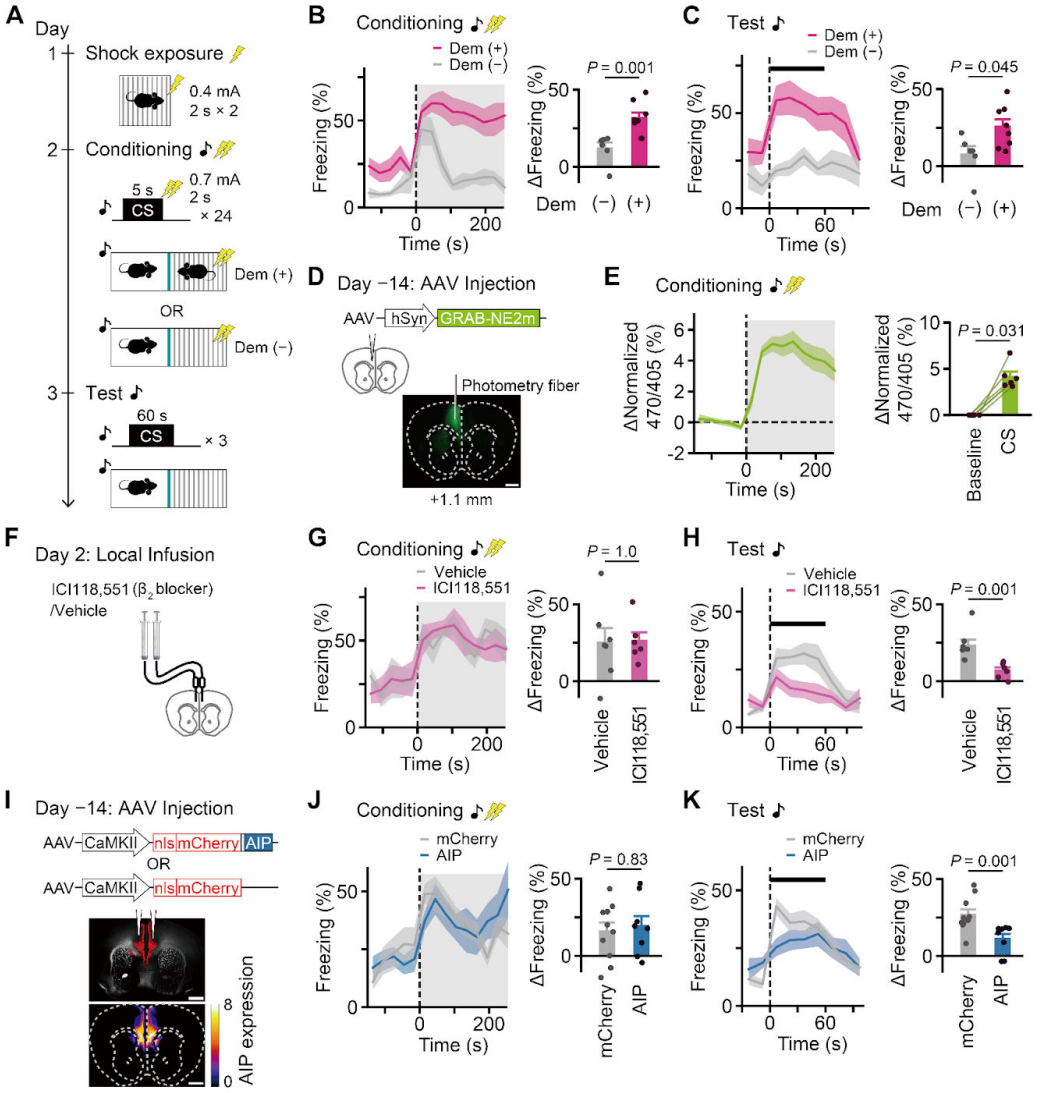

Figure 4. Noradrenaline and plasticity-related signaling in observational fear learning.

A, Schematic of the experimental timeline of observational fear learning.

B, Traces (left) and plots (right) of freezing on day 2. Grey shade indicates the conditioning period. The changes in freezing during the conditioning periods compared to the baseline periods on day 2 were plotted.

C, Traces (left) and plots (right) of freezing on day 3. Averaged freezing responses over the CS presentations are shown, and the bar indicates the CS period. The changes in freezing during the CS periods compared to the baseline periods on day 3 were plotted.

D, Schematic of the virus injection and fiber photometry experiment in the mPFC (top) and representative image showing fluorescence of GRAB-NE_{2m} (green) (bottom). The trace of fiber was overlaid on the image. Scale bar, 1 mm.

E, Traces (left) and plots (right) of GRAB-NE_{2m} fluorescence on day 2.
F, Schematic of cannula injection of ICI118,551 (β_2 inverse agonist). The experimental timeline of observational fear learning is the same as (A).
G, H, Traces and plots of freezing on day 2 (G) and on day 3 (H) in mice with injections of ACSF or ICI118,551 on day 2.
I, Images showing the spread of AIP expression. Representative (top) and the average of mCherry fluorescences after binarization from all the mice used in behavioral experiments (n = 8 mice) are shown. Scale bar, 1 mm.
J, K, Traces and plots of freezing on day 2 (J) and on day 3 (K) in mice injected with mCherry or AIP.
Mann–Whitney U test for (B, C, G, H, J, K). Wilcoxon signed-rank test for (E).
Error bars and shades indicate S.E.M.

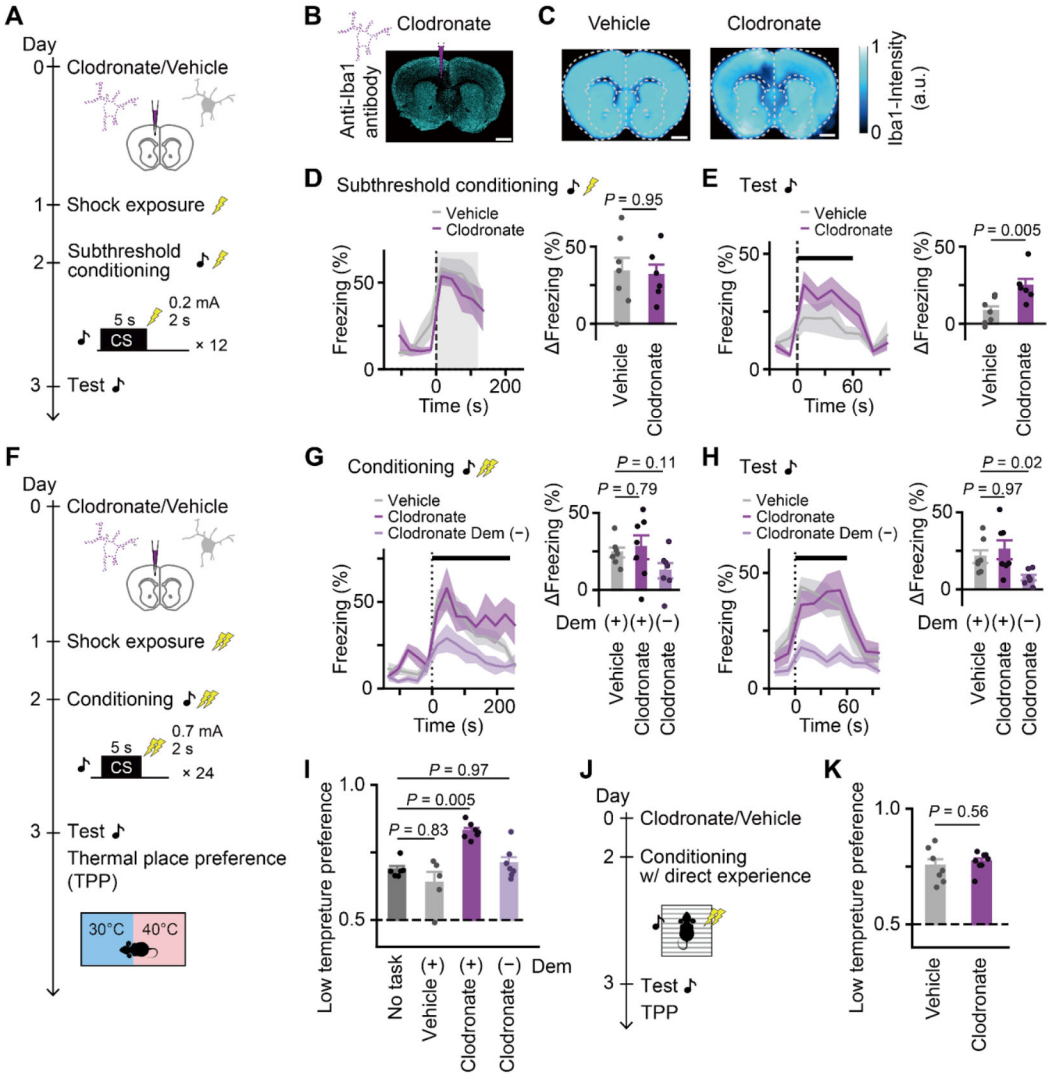

Figure 5. Microglial protection of cross-talk between emotional circuits.
A, Schematics of experimental timeline for subthreshold observational fear learning.
B, Representative image showing Iba1 immunoreactivity in clodronate injected brain. Scale bars, 1 mm.
C, Averaged images showing Iba1 immunoreactivity in the vehicle (left) and clodronate (right) injected brain. Averaged images were generated from all the brains used in behavioral experiments shown in (D) and (E). Dark color indicates areas with low Iba1 immunoreactivity. Scale bars, 1 mm.
D, E, Traces and plots of freezing on day 2 (D) and on day 3 (E) in mice with injections of vehicle or clodronate in subthreshold observational fear learning.
F, Schematic of experimental timeline for observational fear learning and subsequent thermal place preference test.

G, H, Traces and plots of freezing on day 2 (G) and on day 3 (H) in mice with injections of vehicle or clodronate in observational fear learning, and in mice with injections of clodronate without demonstrator.
I, Plots of thermal preference place after observational fear learning. Data for “No task” are the same as that shown in Supplementary Figure 9G.
J, Schematic experimental timeline for direct fear learning and subsequent thermal place preference test.
K, Plots of thermal place preference test after direct fear learning.
Error bars and shades indicate S.E.M.
Mann–Whitney U test for (D, E, K), Kruskal–Wallis test and post hoc Steel’s test for (G, H, I). P = 0.13, 0.0027, and 0.0027 for Kruskal–Wallis test in (G, H, I).

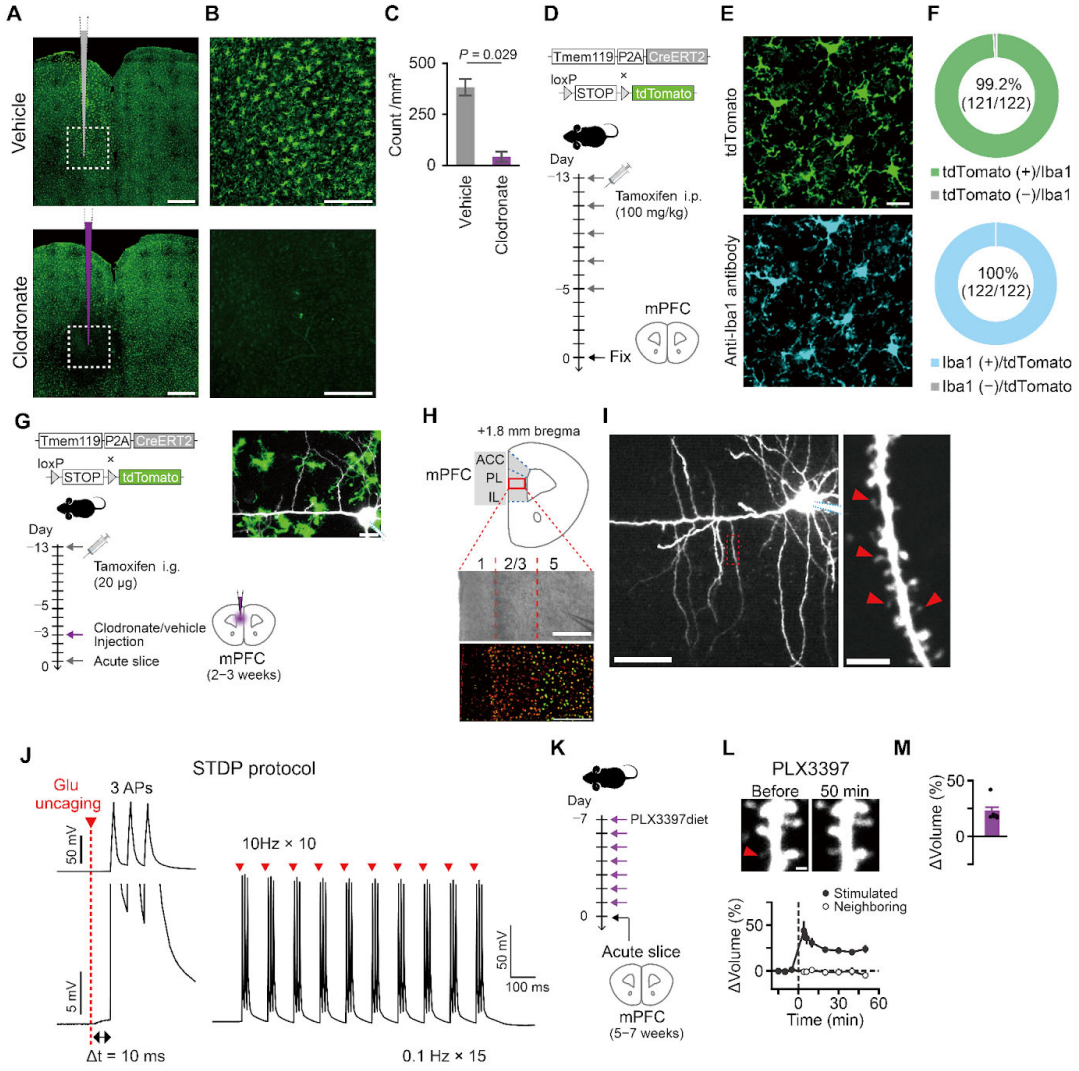

Supplementary Figure 1. Ablation of microglia and STDP stimulation.

A,B, Representative images of confocal microscopy showing anti-Iba1 fluorescence in low magnification (A) and high magnification (B) in brains 2 days after vehicle injection (top) and clodronate injection (bottom). Scale bars, 500 μm (A) and 200 μm (B). Dashed lines indicate the areas shown in high magnification.

C, Plots of microglial counts in the magnified areas shown in (A) and (B) 1–2 days after the injection. n = 4 mice per each condition. Mann–Whitney U test.

D, Schematic of the experimental timeline in transgenic mice.

E, Representative confocal microscopy images showing anti-Iba1 and tdTomato fluorescences. Scale bars, 20 μm.

F, Charts of cell counts from slices of 6 mice.

G, Schematic of the experimental timeline for microglial ablation in juvenile mice.

H, Schematics of a coronal slice containing the mPFC (top), and images showing electrode positioning (middle) and immunohistochemical labeling of cortical layers with Satb2 (red) and Ctip2 (green) (bottom). Neurons in the anterior cingulate cortex (ACC), prelimbic cortex (PL), or infralimbic cortex (IL) were recorded. Scale bars, 200 μm.
I, Images of a pyramidal neuron (left) and dendritic spines (right) obtained by 2-photon microscopy. Red arrows indicate typical spines stimulated by uncaging. Scale bars, 50 μm (left) and 5 μm (right).
J, Traces of membrane potential during one burst (left) and one train (right) of stimulation in STDP protocols. Action potentials (APs) were evoked by pulsed current injections (1.5−2.0 nA, 2 ms).
K, Schematic of experimental timeline. adolescent mice were fed PLX3397 containing chow (100 mg/kg of chow) for 7 days.
L, Representative images of dendrites before and 50 minutes after STDP stimulation (top) and time courses of spine volumes (bottom). Red arrows indicate stimulated spines. Scale bars, 1 μm.
M, Plots of spine volume changes.
Error bars represent S.E.M.

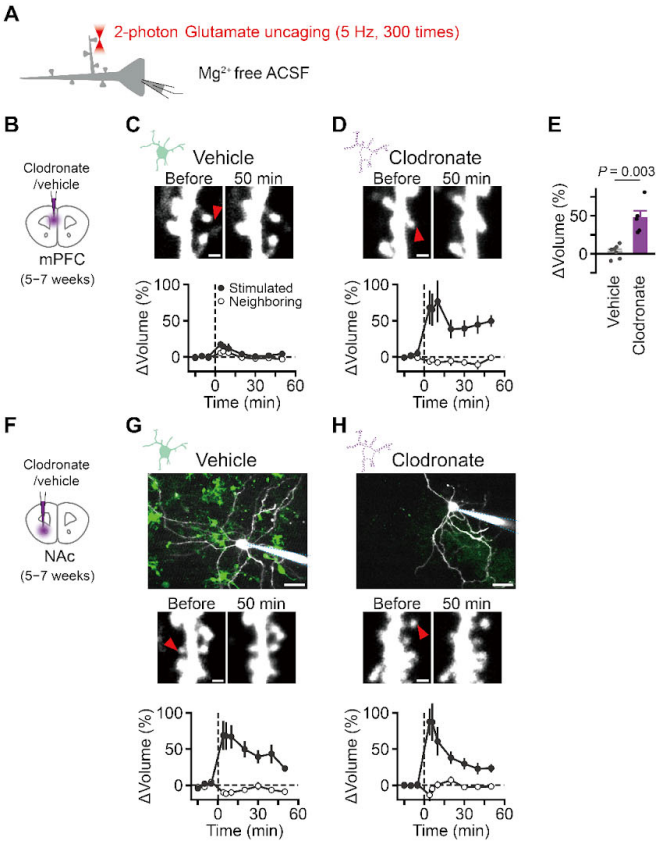

Supplementary Figure 2. Spine enlargement in magnesium-free condition.
A, Schematic of the experimental configuration for two-photon uncaging on dendritic spines of a pyramidal neuron under Mg^{2+}-free conditions. Whole-cell recordings were made to confirm uncaging-induced EPSCs, but action potentials were omitted during plasticity induction.
B, Schematic of clodronate or vehicle injection in adolescent mice (5−7 weeks old).
C,D, Representative images of dendrites before and 50 minutes after STDP stimulation (top) and time courses of spine volumes (bottom) in the slices with vehicle (C) and clodronate (D) injections. Scale bars, 1 μm.
E, Plots of spine volume changes.
F, Similar to (B) but injections and experiments were performed in the nucleus accumbens (NAc).
G,H, Representative images of acute slices in the NAc from Tmem119-CreERT2; Ai14 mice (top) and dendrites before and 50 minutes after STDP stimulation (middle) and time courses of spine volumes (bottom) in the slices with vehicle (G) and clodronate (H) injections. Scale bars, 20 μm (top) and 1 μm (middle).
Error bars represent S.E.M.

Red arrows indicate stimulated spines.
Statistical analysis was performed using the Mann–Whitney U test in (e).

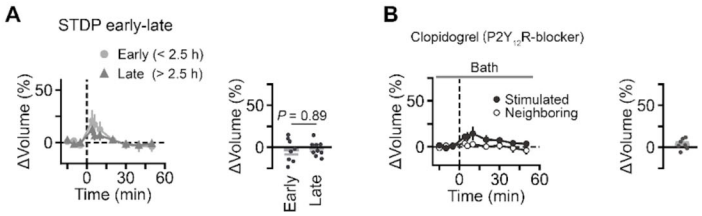

Supplementary Figure 3. Effects of acute slice preparation.
A, Time courses of spine volumes before and after 2.5 hours of slice preparation (left) and plots of spine volume changes (right). Data from Figure 1F and Figure 3B were reanalyzed. Incubation times at the time of STDP stimulation were 2.4 ± 0.2 h and 4.5 ± 0.9 h (mean ± SD), respectively. Statistical analysis was performed using the Mann–Whitney U test.
B, Time courses of spine volumes (left) and plots of spine volume changes (right) in the presence of Clopidogrel (10 μM, $P2Y_{12}$ receptor antagonist). Gray bars indicate the periods for bath application.

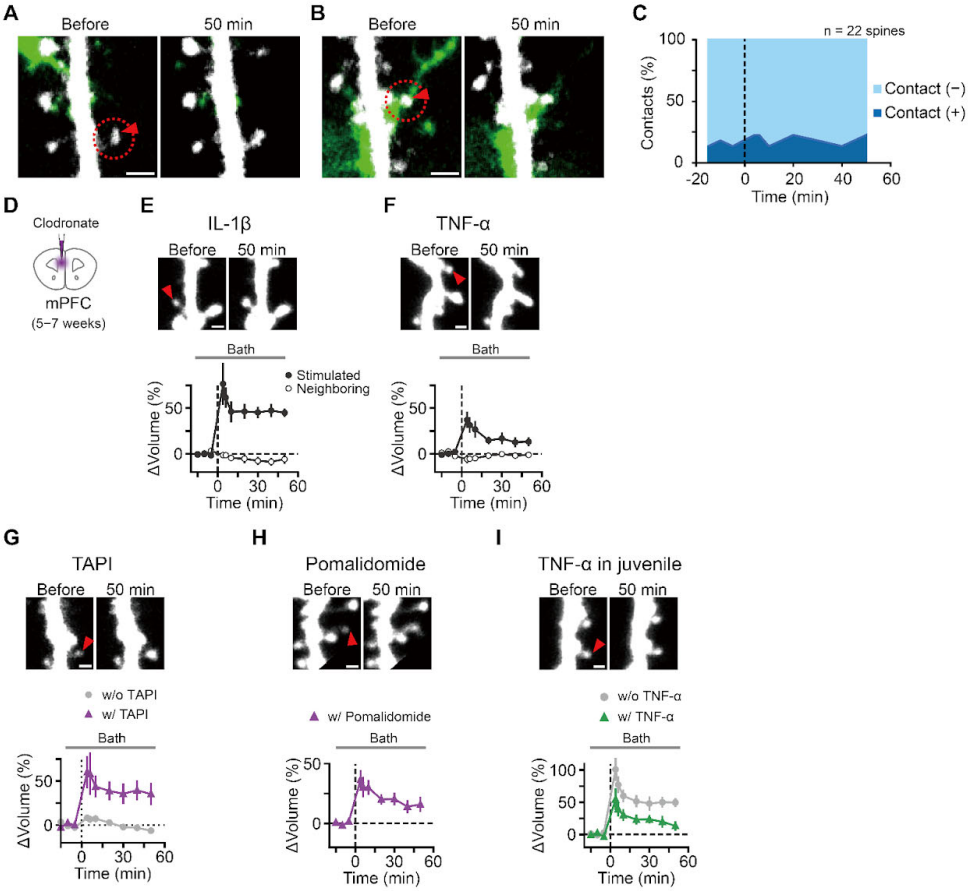

Supplementary Figure 4. Microglial downstream signaling.
A, Representative images showing the absence of microglia (green) near the stimulated spine before and after STDP stimulation. The absence of contact was defined by the lack of green signal (within 3 S.D. of a reference background area) in the regions-of-interest (red dashed circle, 4 μm in diameter centered on the stimulated spine) in the 4 μm z-stack image.
B, Representative images of microglia located near the stimulated spine.
C, Plots showing the proportion of microglial contacts with stimulated spines over time.
D, Schematic of clodronate injection in adolescent mice (5−7 week old).
E,F, Representative images of dendrites before and 50 minutes after stimulation (top) and plots of spine volumes (bottom) in the slices with clodronate injections in the presence of IL-1β (1 ng/ml, bath) (E) and TNF-α (10 nM, bath) (F).
G, H, Representative images and plots of spine volume changes in the presence of the TAPI-0 (1 μM, bath) (G) and Pomalidomide (100 μM, bath, TNF-α receptor inhibitor) (H) in adolescent mice.
I, Representative images and plots of spine volume changes in the presence of TNF-α (10 nM, bath) in juvenile mice (2−3 weeks old).

Red arrows indicate stimulated spines. Scale bars, 2 μm in (A, B), 1 μm in (E, F, G, H, I). Error bars represent S.E.M.

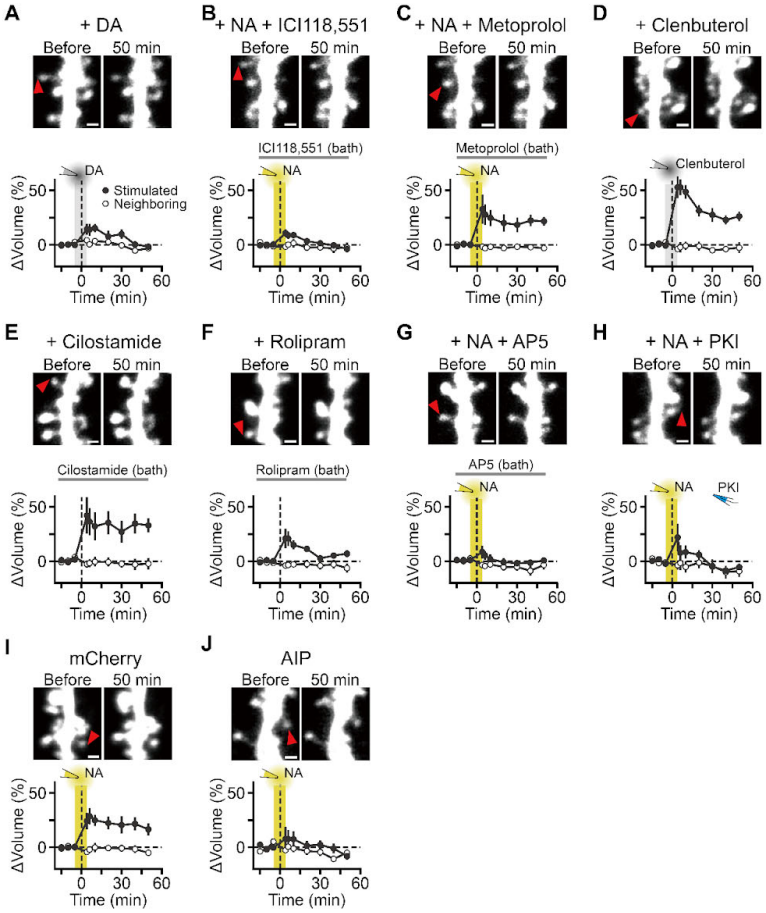

Supplementary Figure 5. Pharmacological studies on spine enlargement in the mPFC.

A–**H,** Representative images of dendrites before and 50 minutes after stimulation (top) and time courses of spine volumes after STDP stimulation (bottom) in the presence of (A) dopamine (DA), (B) NA and a β_2 blocker, (C) NA and a β_1 blocker, (D) a β_2 agonist, (E) PDE3 inhibitor, (F) PDE4 inhibitor, (G) NA and AP5, and (H) NA and PKI. Shading indicates the periods of puff application for DA, NA or a β_2 agonist. Gray bars indicate the periods for bath application. Error bars represent standard error. Filled and open symbols represent spine volumes measured from stimulated spines and unstimulated neighboring spines (control), respectively. Red arrows indicate stimulated spines.

I, J, Representative images of dendrites before and 50 minutes after stimulation (top) and time courses of spine volumes (bottom) in the absence (I) and presence (J) of AIP. Scale bars, 1 μm. Error bars represent S.E.M.

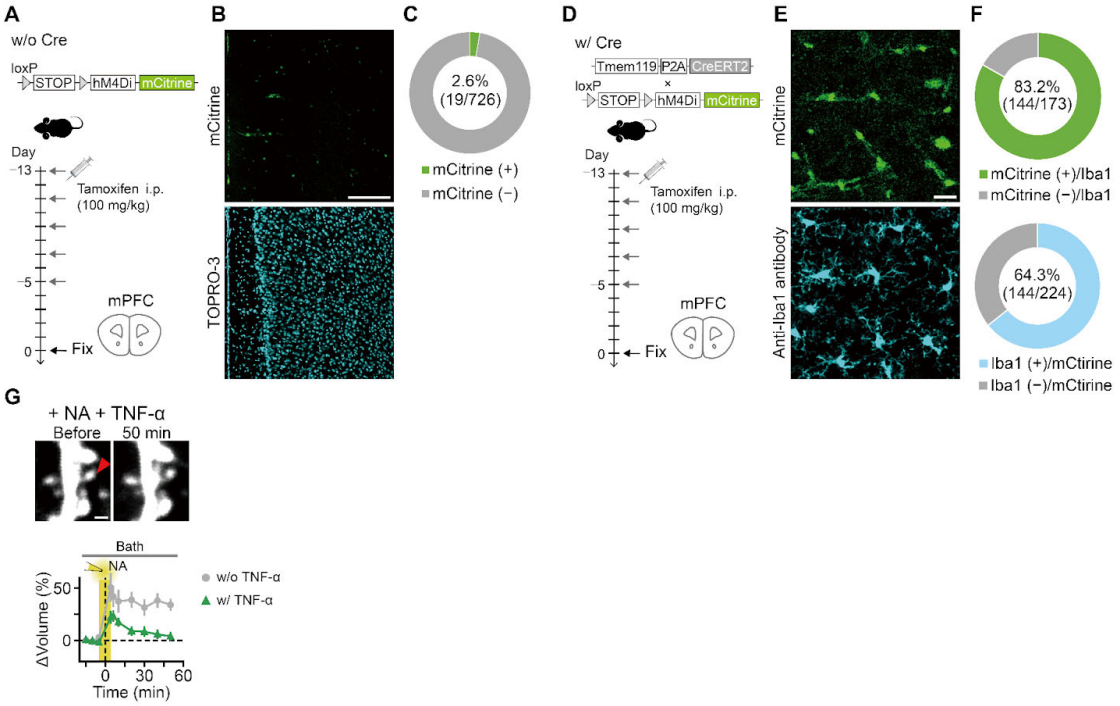

Supplementary Figure 6. Chemogenetic manipulation of microglia.
A, Schematic of the experimental timeline in mice without the Cre-driver.
B, Images showing mCitrine fluorescence (top) and nuclear staining with TOPRO-3 (bottom) in mice without the Cre-driver.
C, Chart showing proportion of mCitrine expressing cells out of TOPRO-3 positive cells. Data were obtained from slices of 2 mice.
D, Schematic of experimental timeline in mice with Cre-driver.
E, Images showing mCitrine fluorescence (top) and immunostaining with anti-Iba1 antibody (bottom) in mice with Cre-driver.
F, Chart showing proportion of the mCitrine expressing cells out of anti-Iba1 positive cells (top) and anti-Iba1 positive cells out of mCitrine expressing cells (bottom). Slices from 6 mice.
G, Representative images of dendrites before and 50 minutes after STDP stimulation (top) and time courses of spine volumes (bottom) with or without TNF-α (10 nM, bath) in the presence of NA (50 μM). Red arrows indicate stimulated spines.
Scale bars, 200 μm in (B), 20 μm in (E), and 1 μm in (G).
Error bars represent S.E.M.

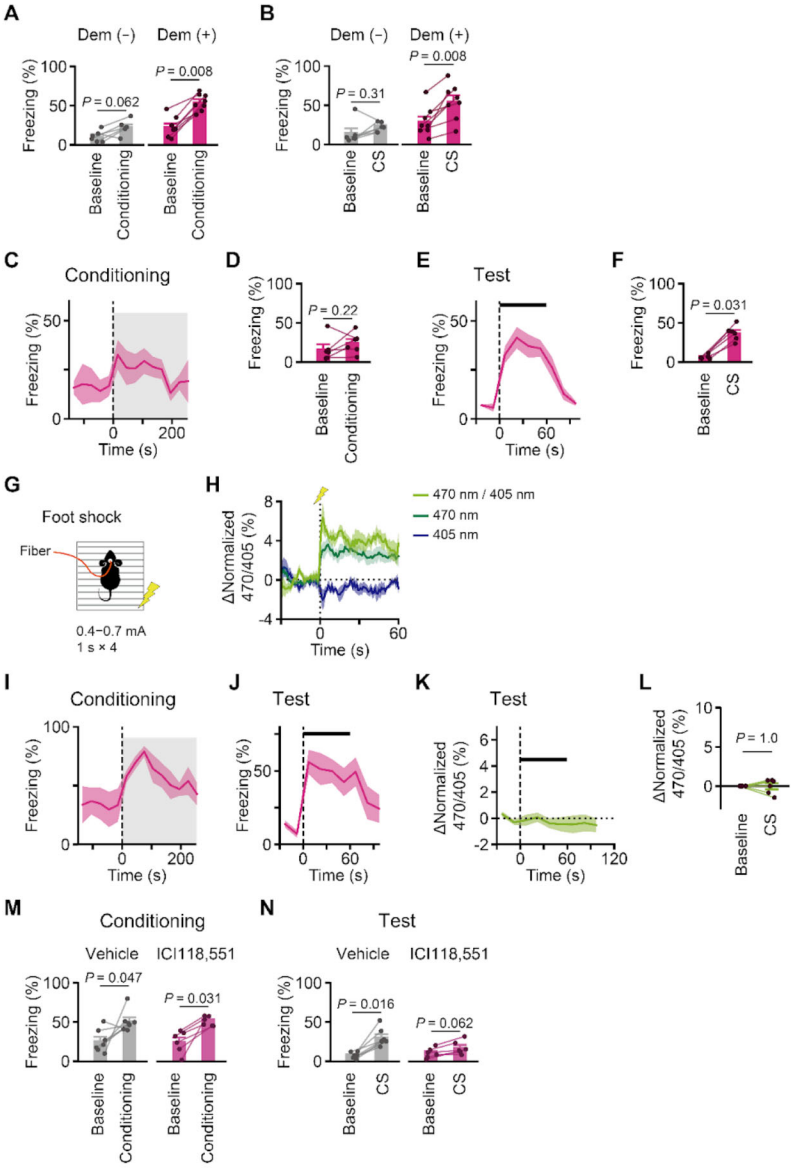

Supplementary Figure 7. Observational fear learning.
A, B, Plotsof freezing on day 2 of conditioning (A) and day 3 of test (B) of mice conditioned with or without demonstrator.
C−F, Traces (C,E) and plots (D,F) of freezing on day 2 of conditioning (C,D) and day 3 of test (E,F) in female mice. A pair of female mice was used for observer and demonstrator.
G, Schematic of photometry recording in response to foot shock (0.4−0.7mA, 1 s).
H, Traces of raw fluorescences (signals obtained by excitation with 405 nm LED or 470 nm LED) and ratio (470 nm/405 nm) against the onset of the foot shock. Average of 4 trials are shown. Note that the isosbestic wavelength of the probe is around 410 nm [78]

and therefore the signal with 405 nm excitation exhibited the opposite direction to that of 470 nm excitation. These mice were a separate set from those used in observational fear learning.

I,J, Traces of freezing on day 2 (I) and day 3 (J) in fiber photometry recording experiment.

K,L, Trace (K) and plots (L) of GRAB-NE_{2m} fluorescence on day 3.

M,N, Plots of freezing on day 2 (M) and on day 3 (N) in ICI118,551 experiments.

Wilcoxon signed-rank test for (A, B, D, F, L, M, N).

Error bars and shades indicate S.E.M.

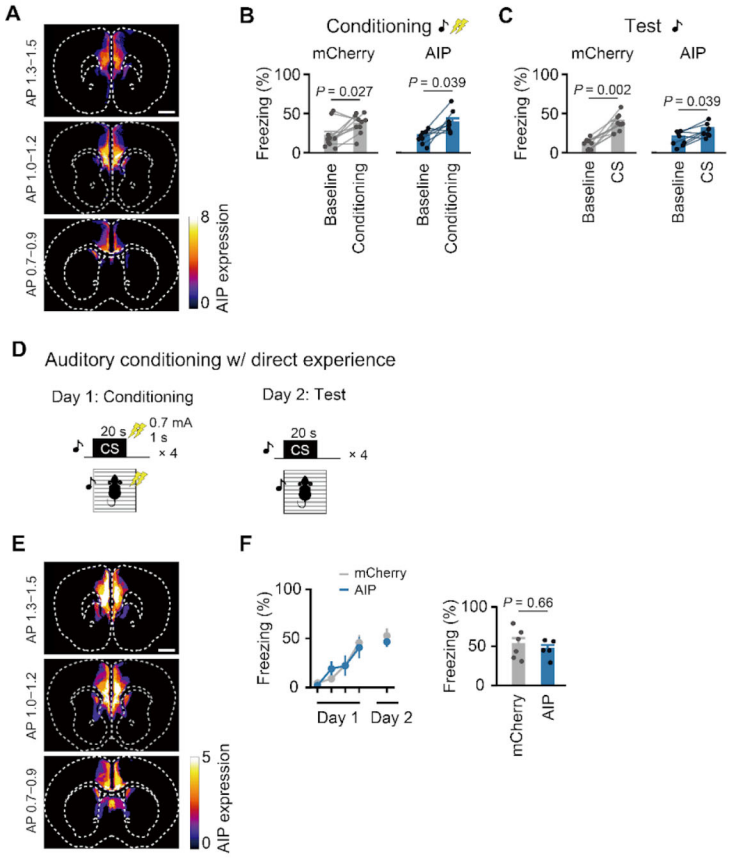

Supplementary Figure 8. Inhibition of CaMKII signaling in fear learning.
A, Images showing averaged intensity of AIP expression in all the mice engaged in the observational fear learning. AP indicates anteroposterior coordinates from the bregma in mm.
B, C, Plots of freezing on day 2 (B) and on day 3 (C) in AIP experiments.
D, Schematic of auditory conditioning with direct fear experience.
E, Images showing averaged intensity of AIP expression in all the mice engaged in auditory conditioning with direct fear experience.
F, Time courses of freezing on day 1 (conditioning) and on day 2 (test) (left) and plots on day 2 (right). Freezing responses during tone periods (20 s) are shown for each trial (day 1) or average of 4 trials (day 2).
Scale bars in (A, E) indicate 1 mm.
Wilcoxon signed-rank test for (B,C), Mann–Whitney U test for (F).

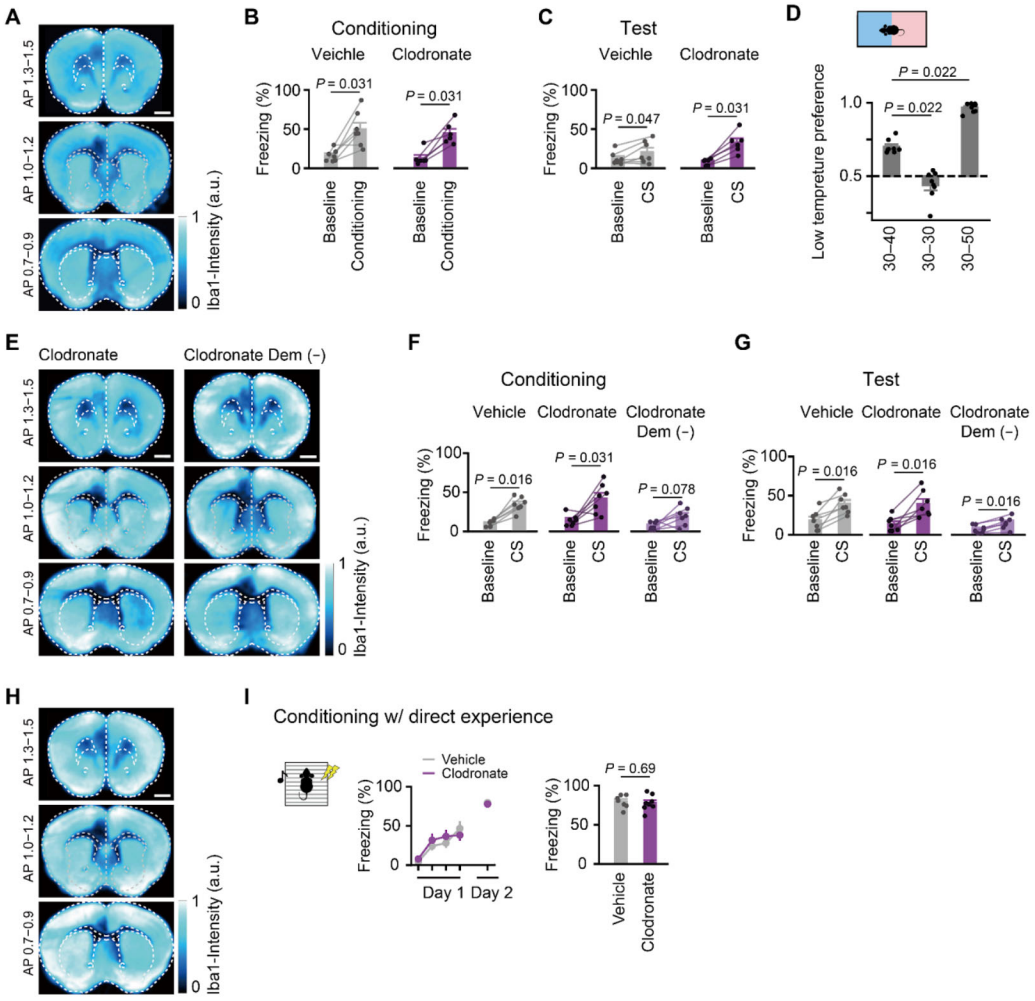

Supplementary Figure 9. Ablation of microglia in fear learning.
A, Images showing averaged intensity of Iba1 immunoreactivity in the brain from all the clodronate-injected mice used for subthreshold conditioning.
B,C, Plots of freezing on day 2 (B) and on day 3 (C) in subthreshold conditioning.
D, Thermal place preference with various temperatures. Times spent in the lower temperature plate during the latter 5 min out of total 10 min recording periods are shown**.**
E, Images of Iba1 immunoreactivity from all the mice used for conditioning and thermal place preference test.
F, G, Plots of freezing on day 2 (F) and on day 3 (G) in conditioning with clodronate injections with and without demonstrator.
H, Images of Iba1 immunoreactivity from all the mice used for conditioning with direct experience.
I, Auditory fear conditioning with direct experience in the presence and absence of

clodronate.
Scale bars in (A, E, H) indicate 1 mm. Wilcoxon signed-rank test for (B,C, F, G), Wilcoxon signed-rank test with Bonferroni correction after Friedman test ($P < 0.001$) for (D), Mann–Whitney U test for (I).